Geochemistry Geophysics Geosystems G3

Article
Volume 14, Number 3
27 March 2013
doi:10.1029/2012GC004392
ISSN: 1525-2027

Published by AGU and the Geochemical Society

# Spatial and temporal patterns of Cenozoic dynamic topography around Australia

**K. Czarnota**
*Bullard Laboratories, Madingley Rise, Madingley Road, Cambridge, CB30EZ, UK*
*Geoscience Australia, GPO Box 378, Canberra, ACT, 2601, Australia*
*(kc394@cam.ac.uk)*

**M. J. Hoggard and N. White**
*Bullard Laboratories, Madingley Rise, Madingley Road, Cambridge, CB30EZ, UK*

**J. Winterbourne**
*BP Exploration Operating Co. Ltd, Sunbury-on-Thames, Middlesex, TW167BP, UK*

[1] Despite its importance, the spatial and temporal pattern of dynamic topography generated by mantle convective circulation is poorly known. We present accurate estimates of dynamic topography from oceanic basins and continental margins surrounding Australia. Our starting point is measurement of residual depth anomalies on the oldest oceanic floor adjacent to the continental shelf. These anomalies were determined from a combined dataset of ~200 seismic reflection and wide-angle images of well-sedimented oceanic crust. They have amplitudes of between −1 km and +0.5 km, and their spatial variation is broadly consistent with long-wavelength free-air gravity and shallow seismic tomographic anomalies. Along the Northwest Shelf, a regional depth anomaly of −300 to −700 m intersects the adjacent continental shelf. The temporal evolution of this anomaly was determined by analyzing the stratigraphic architecture of an extensive carbonate platform, which fringes the shelf and records a dramatic switch from progradation to aggradation during Neogene times. Three-dimensional seismic mapping calibrated by boreholes was used to calculate water-loaded subsidence histories at rollover points of clinoforms along the shelf. At 9 ± 3 Ma, the rate of subsidence increases from 5 to up 75 m $Myr^{-1}$, generating a subsidence anomaly of −300 to −700 m. The amplitude of this anomaly varies along the shelf and cannot be generated by glacio-eustatic sea-level variation. Instead, we propose that a regional subsidence episode, which affects both the proximal shelf and the distal oceanic basin, was generated by convective drawdown. By combining our results with other published estimates of uplift and subsidence, a map of Australia, which shows the spatial and temporal pattern of dynamic topography is presented. Most, but not all, of Australia's epeirogeny can be attributed to rapid northward motion of the Australian plate over a pre-existing pattern of convective circulation.

**Components:** 15,600 words, 16 figures, 2 tables.

**Keywords:** Dynamic topography; sea level; Australia; Neogene

**Index Terms:** 8120 Dynamics of lithosphere and mantle: general; 1641 Sea level change; 9330 Australia

**Received** 20 September 2012; **Revised** 20 December 2012; **Accepted** 20 December 2012; **Published** 27 March 2013.

Czarnota K., M. J. Hoggard, N. White, and J. Winterbourne (2013) Spatial and temporal patterns of Cenozoic dynamic topography around Australia, *Geochem. Geophys. Geosyst.*, *14*, 634–658, doi:10.1029/2012GC004392.

© 2013 American Geophysical Union. All Rights Reserved.

## 1. Introduction

[2] It is generally agreed that plate motion is maintained by convective circulation of the Earth's mantle [e.g., *Schubert et al*., 2001]. However, the detailed spatial and temporal pattern of this circulation is poorly known. A fruitful way forward relies on the fact that convection should generate transient vertical motion (i.e., dynamic topography) at the Earth's surface. Thus, accurate measurements of dynamic topography through space and time could greatly improve our quantitative understanding of hitherto inaccessible details of mantle convection. In recent years, greater emphasis has been placed on building and applying global models which predict the spatial and temporal variation of dynamic topography [e.g., *Hager*, 1984; *Hager and Richards*, 1989; *Cazenave et al*., 1989; *Lithgow-Bertelloni and Gurnis*, 1997]. To some extent, these predictive models have been tested using present-day observations of dynamic topography [e.g., *Lithgow-Bertelloni and Gurnis*, 1997; *Gurnis et al*., 1998; *Moucha et al*., 2008]. Nevertheless, the observational database is sparse and lags behind the sophistication of modern modeling algorithms [*Burke*, 1996; *Wheeler and White*, 2000; *Winterbourne et al*., 2009].

[3] This lack of accurate observations arises from the difficulty in isolating reliable dynamic topographic signals. Topography and bathymetry are primarily controlled by the density structure of the crust and lithospheric mantle which are poorly known. In the oceanic realm, this difficulty can be circumvented since long-wavelength subsidence is controlled by cooling and thickening of the oceanic lithosphere in accordance with a well-established age-depth relationship [*Parsons and Sclater*, 1977; *Crosby et al*., 2006]. This relationship holds for the subsidence of oceanic lithosphere, which is unaffected by dynamic topography. Elsewhere, careful estimates of age and depth can be used to identify and measure positive and negative residual depth anomalies which are attributable to spatial variations of present-day dynamic topography. Residual depth anomalies of the oldest oceanic lithosphere, which abuts continental shelves, can be used to predict the amplitude and wavelength of dynamic topography along these shelves. These predictions can be tested by analyzing stratigraphic records along continental margins, which may indirectly preserve the temporal history of dynamic topography.

[4] This study focusses on dynamic topography of the Australian plate and its Northwest Shelf. The Australian plate is a useful natural laboratory for three reasons. First, Australia is surrounded by extensional passive margins which are unaffected by plate boundary shortening (Figure 1). Second, the gradient of Neogene post-rift thermal subsidence at the western and southern margins is small since sea-floor spreading began over 80 Ma [*Müller et al*., 2008]. Third, Australia has been the fastest moving continent since the Eocene and straddles the southern edge of an important positive geoid anomaly [*Sandiford*, 2007]. Consequently, it is an ideal candidate to investigate the interplay between plate motion and convective circulation.

[5] We are particularly interested in examining links between the pattern of present-day dynamic topography and Neogene observations of vertical motions recorded at continental margins. To investigate these links, we first determine the present-day dynamic topography by calculating residual depth anomalies of old oceanic lithosphere adjacent to the continental margin. We then analyze the stratigraphic architecture of the Northwest Shelf where excellent three-dimensional imaging of an extensive carbonate platform provides an important opportunity to investigate how regional residual depth anomalies develop. Finally, we combine our suite of spatial and temporal observations with a review of published constraints to investigate the causes of Australian epeirogeny.

## 2. Residual Topography of Oceanic Lithosphere

[6] The subsidence history of cooling and thickening oceanic lithosphere as it spreads away from a mid-oceanic ridge is well known [e.g., *Parsons and Sclater*, 1977; *Stein and Stein*, 1992]. In contrast to previous analyses, a recent compilation of age-depth measurements focussed on selected regions of the oceanic plates where dynamic support is negligible by carefully excising oceanic plateaux, which are supported by crustal thickness variations, and regions which have significant long-wavelength gravity anomalies [*Crosby et al*., 2006]. In this way, a global age-depth relationship, uncontaminated by present-day dynamic topography, has been isolated. At a given location, age-depth measurements can be used with confidence to measure positive and negative residual depth anomalies. These anomalies are attributable to dynamic topography [*Crosby and McKenzie*, 2009].

[7] For comparison with the global age-depth relationship, spot measurements of the depth to oceanic basement must be converted into an

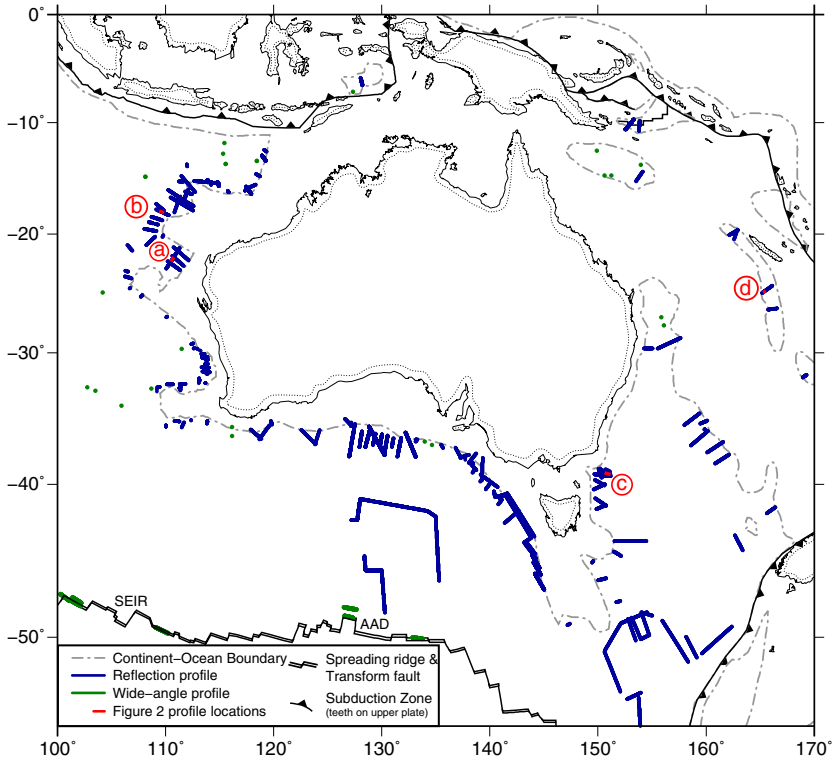


**Figure 1.** Map of region encompassing Australia, which shows seismic reflection/wide-angle lines used in this study. Red letters = location of seismic profiles shown in Figure 2; SEIR = Southeast Indian Ridge; AAD = Australian-Antarctica Discordance. Ocean-continent boundary from *Müller et al*. [2008], *Schellart et al*. [2009], and this study.

equivalent water load. The accuracy of this conversion depends upon thicknesses and densities of the sedimentary column and of the oceanic crust. Published maps of residual topography often use global grids of sedimentary and crustal thicknesses to estimate water-loaded subsidence [*Colin and Fleitout*, 1990; *Panasyuk and Hager*, 2000; *Kaban et al*., 2003; *Steinberge*, 2007; *Crosby and McKenzie*, 2009]. Unfortunately, there are significant errors in existing digital grids, especially on the oldest, highly sedimented oceanic crust [*Crosby et al*., 2011]. *Winterbourne et al*. [2009] showed that accurate spot estimates of residual depth can be obtained from a database of seismic reflection profiles calibrated by modern wide-angle experiments. At continental margins, the oldest bona fide oceanic crust is usually easily identified on seismic reflection profiles and crustal age is obtained from the gridded compilation of *Müller et al*. [2008] and from local studies.

## 2.1. Seismic Database

[8] We exploit a database of deep seismic reflection profiles archived at Geoscience Australia [*Fleming*, 2010]. This database has been supplemented with other published and unpublished datasets to identify 169 deep seismic reflection profiles and 29 reversed wide-angle experiments of different vintages which occur on *bona fide* oceanic crust (Figure 1, Supporting Information 1–3).[1]

[9] The accuracy of residual depth anomaly calculations from seismic reflection profiles depends upon the quality of a given profile. Usually, the sedimentary pile down to the top of oceanic crust is well imaged, and the sedimentary correction can be accurately determined. Around Australia, imaging of the oceanic Moho is patchy. For example, an excellent Moho is imaged along the Northwest Shelf, in the Tasman Sea, and in the Caledonian Basin (Figure 2). However, Moho reflections are weak or absent in the Perth Basin and in the Great Australian Bight. Fortunately, the crustal correction is generally much smaller than the sedimentary correction. Where the Moho is not reliably imaged, we determine either an upper or a lower bound for the amplitude of the residual topographic anomaly from nearby constraints (e.g., regional

[1] All Supporting Information may be found in the online version of this article.

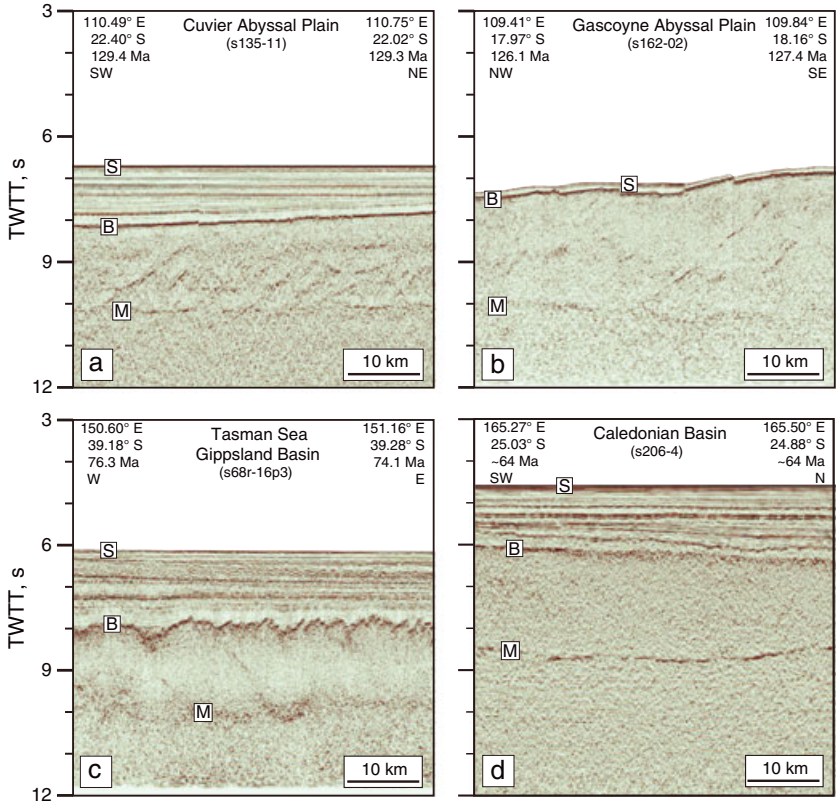


**Figure 2.** Portions of seismic reflection profiles used to calculate residual topography of oceanic lithosphere (see Figure 1). S = seabed; B = sediment-basement interface; M = Moho.

crustal thickness variation from oceanic spreading rates, wide-angle experiments located along strike, and the presence or absence of oceanic plateaux and seamounts).

[10] The accuracy of residual topographic estimates made from seismic wide-angle experiments depends upon the vintage of the experiment and on the modeling technique used [*White et al.*, 1992]. The best estimates are from modern, dense wide-angle surveys, which match synthetic seismograms by forward or inverse modeling [e.g., *Holmes et al.*, 2008]. *White et al.* [1992] showed that older wide-angle surveys, which use slope-intercept methods, generally underpredict crustal thickness by ~20% and therefore yield upper estimates of residual topography.

## 2.2. Methodology

### 2.2.1. Isostatic Corrections

[11] In order to convert spot measurements of the depth to oceanic basement into an equivalent water load, it is necessary to carry out sedimentary and crustal thickness corrections, which require the density and thickness of both layers to be determined. The sedimentary correction, $C_s$, converts a column of sediment into an equivalent column of water so that

$$C_s = \left(\frac{\rho_a - \bar{\rho_s}}{\rho_a - \rho_w}\right) z_s, \quad (1)$$

where $\rho_a$ is the density of the asthenosphere, $\rho_w$ is the density of water, $\bar{\rho_s}$ is the average density of the sedimentary column, and $z_s$ is the thickness of the sedimentary column (Table 1). The crustal thickness correction, $C_c$, normalizes crustal thickness variations to a global oceanic crustal thickness average of 7.1 km so that

$$C_c = \left(\frac{\rho_a - \bar{\rho_c}}{\rho_a - \rho_w}\right)(z_c - 7.1), \quad (2)$$

where $z_c$ and $\bar{\rho_c}$ are the thickness and average density of oceanic crust, respectively [*White et al.*, 1992].

### 2.2.2. Thickness and Density Estimates

[12] To convert from two-way travel time to depth, *Winterbourne et al.* [2009] assembled a global set of time-depth measurements from 39 coincident seismic reflection and wide-angle profiles located

**Table 1.** Notation Table

| Symbol | Description | Value | Units |
|---|---|---|---|
| $z$ | Depth | | km |
| $t$ | Two-way travel time | | s |
| $z_s$ | Sediment thickness | | km |
| $z_c$ | Crustal thickness | | km |
| $\bar{\rho}_s$ | Mean local sediment density | | Mg m$^{-3}$ |
| $\rho_{sg}$ | Solid grain density | | Mg m$^{-3}$ |
| $\rho_m$ | Density of lithospheric mantle | 3.3 | Mg m$^{-3}$ |
| $\rho_a$ | Density of asthenospheric mantle | 3.2 | Mg m$^{-3}$ |
| $\rho_w$ | Density of water | 1.01 | Mg m$^{-3}$ |
| $\bar{\rho}_c$ | Mean density of oceanic crust | $2.86 \pm 0.03$ | Mg m$^{-3}$ |
| $v_w$ | Interval pore fluid sonic velocity | 1.5 | km s$^{-1}$ |
| $v_z$ | Interval sediment sonic velocity | | km s$^{-1}$ |
| $v_{sg}$ | Solid grain velocity | | km s$^{-1}$ |
| $\bar{v}_c$ | Igneous oceanic crust velocity | $6.45 \pm 0.25$ | km s$^{-1}$ |
| $\phi$ | Porosity | | Dimensionless |
| $\phi_\circ$ | Initial porosity | | Dimensionless |
| $\lambda$ | Compaction decay length | | km |
| $C_s$ | Correction due to sediment load | | km |
| $C_c$ | Correction due to crustal load | | km |

on well-sedimented oceanic crust (Figure 3a). These measurements form the basis of a simple empirical method for estimating the thickness and average density of the sedimentary pile where borehole data are unavailable. Two-way travel time, $t$, is given by

$$t = 2\int_0^z \frac{dz}{v(z)}, \tag{3}$$

where $v(z)$, the velocity as a function of depth, is given by

$$\frac{1}{v(z)} = \frac{\phi(z)}{v_w} + \frac{1-\phi(z)}{v_{sg}}. \tag{4}$$

$v_{sg}$ is the solid grain velocity, $v_w$ is the pore fluid velocity, and $\phi(z)$ is the porosity [*Wyllie et al.*, 1956]. Since

$$\phi(z) = \phi_\circ \exp\left(\frac{-z}{\lambda}\right) \tag{5}$$

where $\phi_\circ$ is the initial porosity and $\lambda$ is the compaction decay length [*Athy*, 1930], we obtain

$$\frac{t}{2} = \frac{z}{v_{sg}} + \phi_\circ \lambda \left(\frac{1}{v_w} - \frac{1}{v_{sg}}\right)\left\{1 - exp\left(\frac{-z}{\lambda}\right)\right\}. \tag{6}$$

[13] In order to constrain $\phi_\circ$ and $\lambda$, we minimize the misfit between equation (6) and the 39 time-depth pairs. The global minimum occurs at $\phi_\circ = 0.58$ and $\lambda = 4.3$ km. Uncertainty in depth conversion can be determined by varying $\phi_\circ$ and $\lambda$ and establishing an envelope of $t$-$z$ values which fall inside one standard deviation of the observed time-depth pairs. This envelope corresponds to all $\phi_\circ$-$\lambda$ pairs with a misfit value of less than 0.4 (Figures 3a and 3b). We assume that $v_{sg} = 5.5 \pm 0.5$ km s$^{-1}$ which corresponds to a mixture of quartz and clay [*Christensen*, 1982, Supporting Information 9].

[14] Oceanic crustal thickness is calculated using an average velocity of $\bar{v}_c = 6.45 \pm 0.25$ km s$^{-1}$ (Figure 4). This value of $\bar{v}_c$ was estimated using a compilation of 54 velocity profiles determined by waveform modeling of wide-angle seismic data [*White et al.*, 1992]. Since we are primarily concerned with well-sedimented oceanic crust abutting continental margins, we only used velocity profiles for old (> 10 Ma) crust which have higher values of bulk velocity as a result of the compaction and alteration of layer 2 [*Carlson and Herrick*, 1990].

[15] The average density of the sedimentary column, $\bar{\rho}_s$, is given by

$$\bar{\rho}_s = \rho_{sg} + \frac{\phi_0 \lambda}{z}\left(\rho_w - \rho_{sg}\right)\left[1 - \exp\left(\frac{-z}{\lambda}\right)\right], \tag{7}$$

where $\rho_{sg}$ is the solid grain density of quartz and minor clay ($2.65 \pm 0.05$ Mg m$^{-3}$) [*Christensen*, 1982]. The average density of oceanic crust, $\bar{\rho}_c$, is $2.86 \pm 0.03$ Mg m$^{-3}$, based on downhole logging, core samples, and velocity structure [*Carlson and Herrick*, 1990]. A density increase of 0.05 Mg m$^{-3}$ yields a crustal correction of −23 m per kilometer of anomalous thickness.

### 2.2.3. Examples

[16] Figure 5 plots water-loaded subsidence as a function of age for the portions of oceanic crust shown in Figure 2. Subsidence measurements from two adjacent profiles, which image almost coeval oceanic crust located ~450 km apart on the Northwest Shelf, illustrate the importance of accurate sedimentary and crustal corrections. An example from the Cuvier abyssal plain has a water layer of 6.73 s, a sedimentary layer of 1.29 s, and a crustal layer of 2.12 s (Figure 2a). In contrast, an example from the Gascoyne abyssal plain has a water layer of 7.05 s, a sedimentary layer of 0.16 s,

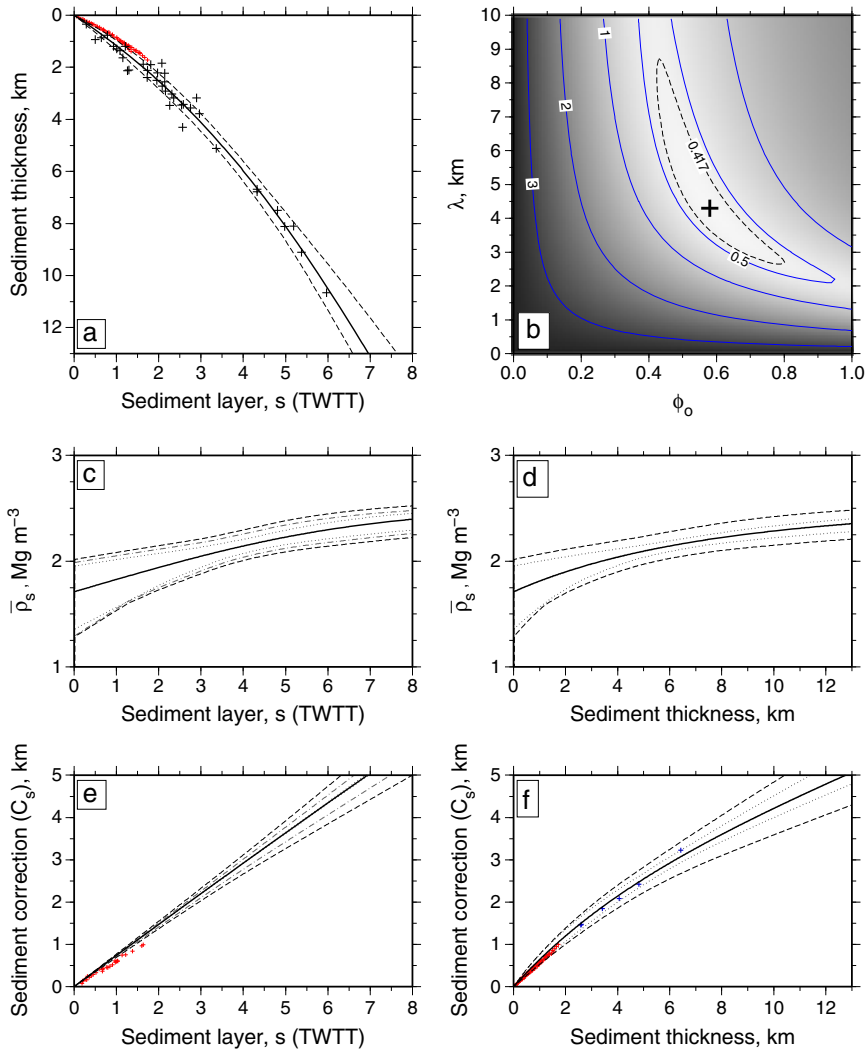


**Figure 3.** Sedimentary correction of oceanic crust. (a) Time-depth measurements used to constrain $\phi_\circ$ and $\lambda$. Black crosses = time-depth pairs from coincident reflection and wide-angle profiles [*Winter-bourne et al.*, 2009]; red crosses = time-depth pairs from deep sea drilling holes [*Crough*, 1983]; black line = best-fit relationship obtained by varying $\phi_\circ$ and $\lambda$; pair of dashed lines = 1$\sigma$ (i.e., misfit of ≤0.417). (b) Root mean square (rms) misfit as function of $\phi_\circ$ and $\lambda$ (equation (6) and Supporting Information). (c–d) Average sediment density as function of time and depth (equation (7)). (e–f) Sedimentary correction as function of time and depth (equation (1)). Solid lines = optimal relationship using values of $\phi_\circ$ and $\lambda$ at global minimum for $v_{sg}$ = 5.5 km s$^{-1}$ and $\rho_{sg}$ = 2.65 Mg m$^{-3}$; dotted lines = error bounds for range of values of $\phi_\circ$ and $\lambda$; dotted/dashed line = error bounds include ±0.5 km s$^{-1}$ uncertainty in $v_{sg}$; outer dashed line = error bounds include ±0.05 Mg m$^{-3}$ uncertainty in $\rho_{sg}$; red/blue crosses = sedimentary corrections of *Crough* [1983] and *Lourens et al.* [2004], respectively.

and a crustal layer of 3.00 s (Figure 2b). If the sedimentary correction is applied, the water-loaded subsidence at each location differs markedly (i.e., 6.0 km on the Cuvier plain, 5.41 km on the Gascoyne plain). When the crustal correction is applied, water-loaded subsidence values change to 5.96 and 5.81 km, respectively.

[17] How reliable are these estimates? The accuracy of our measurements of residual topography is assessed by propagating uncertainties in $\phi_\circ$, $\lambda$, $v_{sg}$, and $\rho_{sg}$ for the sedimentary correction, and in $\bar{v}_c$ and $\bar{\rho}_c$ for the crustal correction (Figures 3 and 4). Residual topographic uncertainty increases as a function of sedimentary and crustal thickness. Increasing compaction gives rise to self-canceling changes in velocity and density and so it is better to determine the sedimentary correction directly from two-way travel time using Figure 3e. Uncertainty in $C_s$ is dominated by variations in the velocity and density of solid grains. Note that the quasi-linear relationship between $t$ and $C_s$ closely

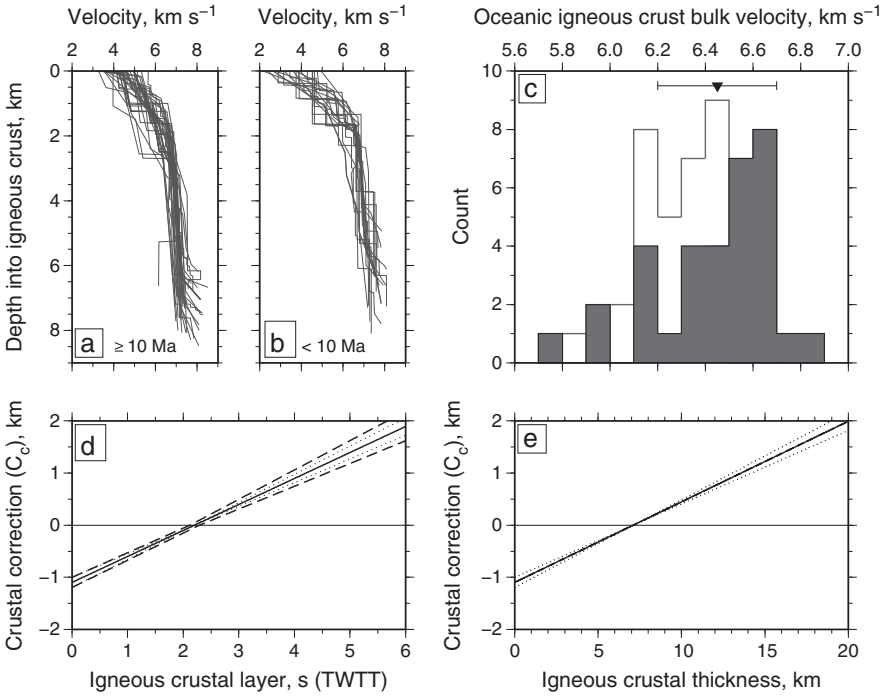


**Figure 4.** Oceanic crustal correction. (a–b) Velocity profiles from old (≥10 Ma) and young (≤10 Ma) oceanic crust. (c) Histogram of bulk velocities for old and young oceanic crust. Inverted triangle with error bar = mean and standard deviation of bulk velocity of old oceanic crust. (d–e) Crustal correction as function of time and depth. Solid line = optimal relationship for $\bar{v}_c = 6.45\,\mathrm{km\,s^{-1}}$ and $\bar{\rho}_c = 2.86\,\mathrm{Mg\,m^{-3}}$; dotted line = error bounds for $\pm 0.03\,\mathrm{Mg\,m^{-3}}$ uncertainty in $\bar{\rho}_c$; dashed line = error bounds include $\pm 0.25\,\mathrm{km\,s^{-1}}$ in $\bar{v}_c$.

resembles the sedimentary loading correction of *Crough* [1983] and *Louden et al.* [2004]. Uncertainty in $C_c$ results from the uncertainty in crustal velocity and average crustal density (Figures 4d and 4e).

[18] The residual topographic anomalies for the Cuvier and Gascoyne abyssal plains are −386 ± 100 m and −261 ± 100 m, respectively. The magnitude of these uncertainties shows that these two estimates of residual topography match within error. The largest sedimentary correction occurs along the western margin of the Tasman Sea where 2.6 s of sedimentary rocks with a bathymetry of 5.0 s and a crustal layer of 1.8 s together give rise to a residual topographic anomaly of −193 ± 174 m. The biggest crustal correction occurs along the Northwest Shelf, where 5.1 s of oceanic crust is overlain by 0.03 s of sediment and 5.8 s of water, which together yields a residual topographic anomaly of −149 ± 227 m. These two examples are the most poorly resolved 0.01° bins in our dataset. In general, the cumulative uncertainty is less than ±100 m (see Supporting Information).

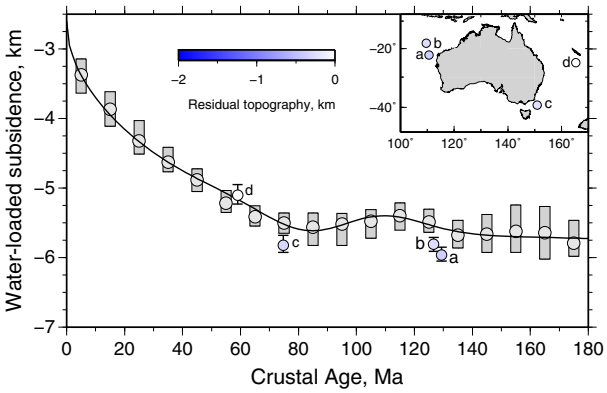


**Figure 5.** Water-loaded subsidence of oceanic lithosphere as function of age. Solid line with gray circles and bars = age-depth relationship uncontaminated by residual depth anomalies [*Crosby et al.*, 2006]. Colored circles with bars = estimates of water-loaded subsidence calculated from profiles shown in Figure 2.

## 2.3. Results

[19] Analysis of 198 profiles shows that most, but not all, oceanic floor surrounding Australia is drawn down with respect to the age-depth curve of *Crosby et al.* [2006]. A circum-Australian transect along the oldest oceanic lithosphere reveals important variations (Figure 6). The most striking anomaly occurs in the Great Australian Bight

which is drawn down by a maximum of 1 km [cf. *Whittaker et al.*, 2010]. The steepest gradient occurs between the South Tasman Rise and the Great Australian Bight where residual topography decreases at a rate of $1\,m\,km^{-1}$. Important gradients are also evident between the Perth and Cuvier abyssal plains. Residual topography is near zero or slightly positive in the Perth abyssal plain and along the South Tasman Rise. In the north, the southern edge of the Argo abyssal plain and the Coral Sea are both drawn down by ~700 m. The most northerly measurements in the Argo abyssal plain are more elevated because they are perched on the flexural bulge of the Java Trench. The height of this bulge is several hundred meters [*Bry and White*, 2007].

[20] Variation of residual topography along the Circum-Australian transect broadly agrees with the pattern of long-wavelength free-air gravity anomalies (Figure 6b). When residual topographic measurements are plotted against long-wavelength anomalies, the slope (i.e., the admittance) is $23 \pm 14\,mGal\,km^{-1}$, which agrees with the admittance value of $30 \pm 5\,mGal\,km^{-1}$ quoted by *Crosby and McKenzie* [2009] for young oceanic crust, based upon unfiltered gravity. An obvious discrepancy occurs in the Perth abyssal plain where a significant negative gravity anomaly occurs. A similar discrepancy was observed along the Brazilian margin by *Winterbourne et al.* [2009]. These discrepancies suggest that deeper density anomalies exist in the mantle which may not produce residual topography. The scatter in the admittance relationship emphasizes that long-wavelength free-air gravity anomalies are only a rough approximation of residual topography. Figure 6c shows that there is limited agreement between the distribution of shear wave velocity anomalies in the top 100 km of the upper mantle and residual topographic anomalies. For example, the residual topographic gradient from the South Tasman Rise to the Great Australian Bight is matched by a shear wave velocity gradient. Correlation between deeper mantle velocity anomalies and residual topography is poor.

[21] A summary map of residual topography is presented in Figure 7. Spot measurements have been supplemented by estimates made from a network of ship-track bathymetry, which was corrected for sediment loading. This network is sparse because we have excluded oceanic plateaux and regions where sedimentary cover exceeds 1.5 km. There is generally good agreement between spot measurements and the ship-track bathymetry.

## 3. Temporal Variation

[22] Our results demonstrate that residual topography of old oceanic lithosphere varies on wavelengths of thousands of kilometers. In the oceanic realm, however, it is not obvious how the growth and decay of residual topography can be measured. Since most of our spot measurements abut continental margins, it should be possible to investigate how residual topography changes by interrogating the record of vertical motions preserved within the stratigraphic architecture of continental shelves. Frequently, clastic and carbonate deposits build out into deeper water and changes in accommodation space are recorded by changes in clinoformal geometry. For example, a rapid increase in accommodation space can be recorded by a change from a progradational to an aggradational pattern of clinoforms. Here, we focus on the stratigraphic architecture of a well-preserved Neogene carbonate platform along the Northwest Shelf of Australia [*Longley et al.*, 2002]. This platform has a strike length of >1500 km, stretching from Cape Range to the Java Trench (Figure 8). It straddles the edge of a long-wavelength drawdown which may be linked to the southeast Asian geoid anomaly [*Sandiford*, 2007]. The present-day shelf break occurs 120–300 km offshore in water depths of 100–300 m.

### 3.1. Stratigraphic Architecture

[23] Over the last 360 Myr, the tectonic history of the Northwest Shelf has been dominated by a series of rifting episodes interspersed with post-rift subsidence and minor shortening events. Its passive margin architecture was created by two rift events which culminated in sea-floor spreading, commencing in the Argo and Gascoyne abyssal plains at ~155 Ma. A ridge jump at ~134 Ma was associated with sea-floor spreading in the Cuvier and Gascoyne abyssal plains (Figure 8) [*Heine and Müller*, 2005]. Post-rift strata were deformed by mild shortening attributed to plate boundary interactions such as Papuan arc-continent collision at ~25 Ma [*Keep et al.*, 1998; *Cathro and Karner*, 2006; *Pigram and Symonds*, 1991]. This shortening often occurred on normal faults adjacent to the current coastline and generally does not affect carbonate clinoformal geometries. A notable exception is Cape Range, an actively growing anticline which initiated in Miocene times and records a minimum of ~300 m of vertical uplift [*Hillis et al.*, 2008].

[24] Total stratigraphic thickness along the margin is >8 km at the present day and Neogene shelf-

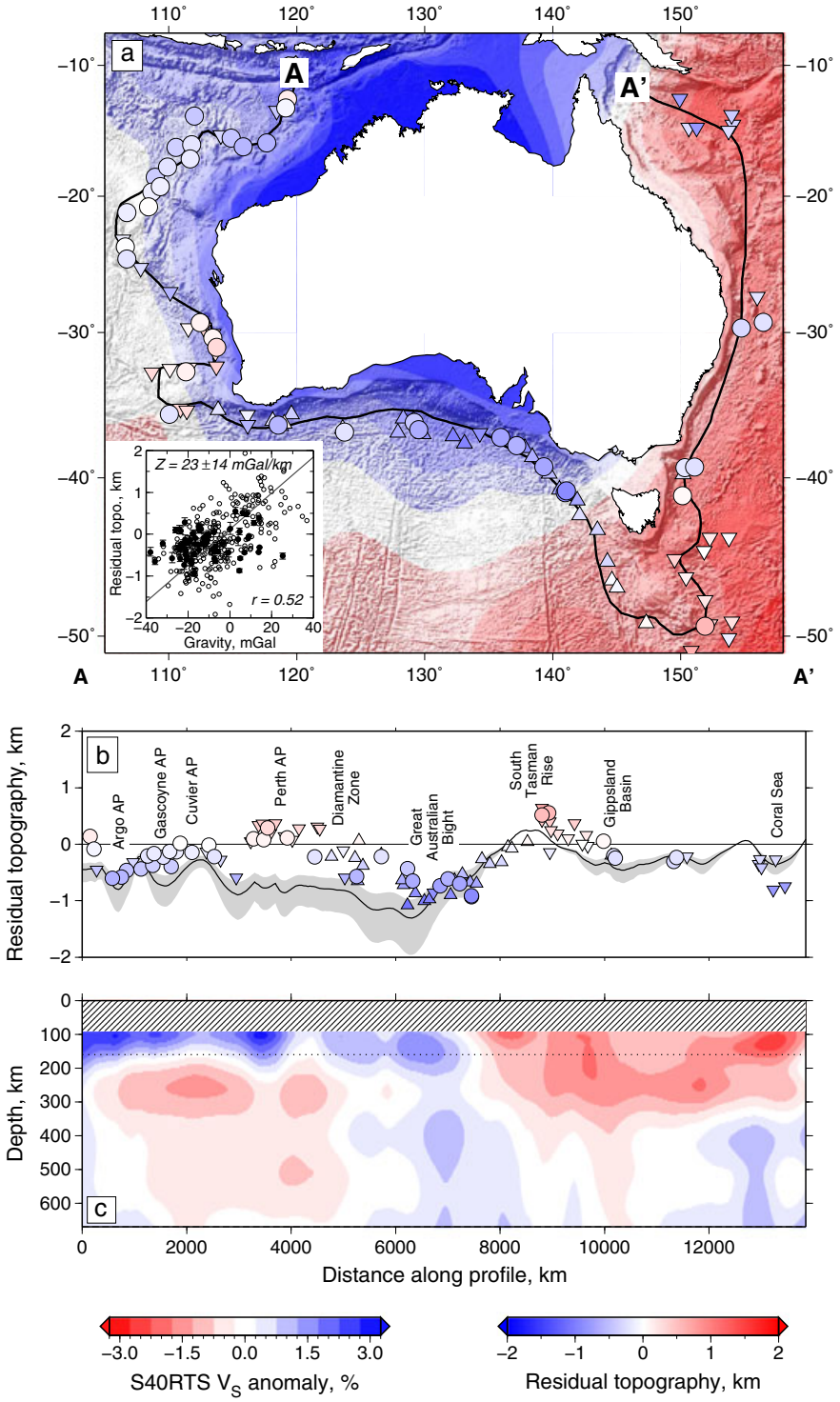


**Figure 6.** (a) Horizontal slice through S40RTS seismic tomographic model of *Ritsema et al*. [2010] at 160 km depth (see color bar at bottom left). Gray background = shaded bathymetry [*Smith and Sandwell*, 1997]; colored circles and upward/downward triangles = accurate estimates and lower/upper bounds of residual bathymetry (see color scale at bottom right). Inset shows residual topography as function of long-wavelength (800–5000 km) free-air gravity anomalies where Z = admittance [*Tapley et al*., 2005]. Solid circles = 61 measurements from this study; open circles = 250 global measurements. (b) Transect A-A′, encircling Australia along oceanic crust. Circles and triangles as before; solid line with gray band = dynamic topography predicted from gravity anomalies using $Z = 30 \pm 10$ mGal km$^{-1}$; AP = Abyssal Plain. (c) Vertical slice through upper mantle from S40RTS model. Hatch pattern = approximate thickness of lithosphere; dotted line = locus of horizontal slice shown in Figure 6a.

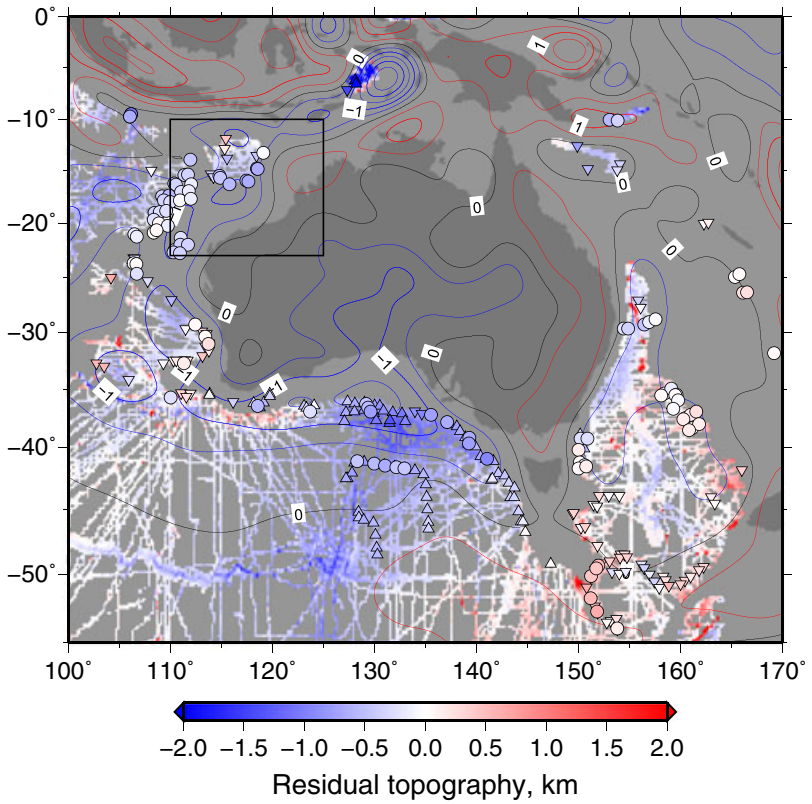


**Figure 7.** Map of residual bathymetry (i.e., dynamic topography) of oceanic lithosphere. Circles and triangles as before, averaged over 1° × 1° cells (see Figure 6). Spider's web of lines = residual bathymetry calculated from selected ship tracks, where sedimentary correction was estimated using the National Geophysical Data Center (NGDC) digital grid [*Divins*, 2008]; band along active and fossil mid-oceanic ridges = residual bathymetry for 0–5 Ma chron; red/black/blue contours = positive/zero/negative contours plotted every 0.5 km of dynamic topography calculated from long-wavelength gravity anomalies assuming $Z = 23$ mGal/km; black box = location of Figure 8. See Supporting Information for further details.

break positions [*Longley et al*., 2002; *Goncharov*, 2004]. Deposition was dominated by siliciclastic rocks until ~85 Ma, by ramp carbonate rocks with subordinate siliciclastic rocks until ~38 Ma, and by predominantly unrimmed open platform clean carbonate rocks from ~30 Ma until the present day (Figure 9) [*Romine et al*., 1997; *Longley et al*., 2002, and references therein]. The switch from siliciclastic to carbonate-dominated deposition is generally attributed to northward drift of the Australian Plate towards warmer water at lower latitudes, a trend which is reflected in faunal assemblages [*Moss et al*., 2004].

[25] Architecture of the carbonate platform changes along strike (Figure 10). The consistent architectural elements across the shelf are two periods of progradation and the loss of a distinct clinoform rollover by ~5 Ma. This loss is associated with transgression and patch reef development slightly inboard of the clinoform rollover position. Carbonate rocks deposited during and after this transgression are equal or greater in thickness compared with those deposited during the preceding 25 Myr. This change indicates an episode of increased subsidence across the margin which is well known and has been attributed to either large-scale intra-plate deformation or to flexural effects associated with the prograding carbonate wedge [*Müller et al*., 2000a; *Kennard et al*., 2003]. Some authors have tried to subdivide Neogene strata into sequences which are then linked to glacio-eustatic sea-level oscillations (Figure 9).

[26] The platform consists of a calcite heterozoan assemblage which is dominated by benthic foraminifera with subordinate bryozoans and corals. Ecostratigraphic analysis of foraminifera from the Dampier Sub-basin by *Moss et al*. [2004] shows that carbonate sediments on top of the platform and at clinoform rollover positions were deposited in neritic paleowater depths (20–200 m). During Middle Miocene times, there is an overall transition from outer to inner neritic water depths (i.e., 100–200 m to 20–100 m). At isolated locations, patch reefs (e.g., Scott Reef, the Rowley Shoals) have continued to grow at or close to sea level,

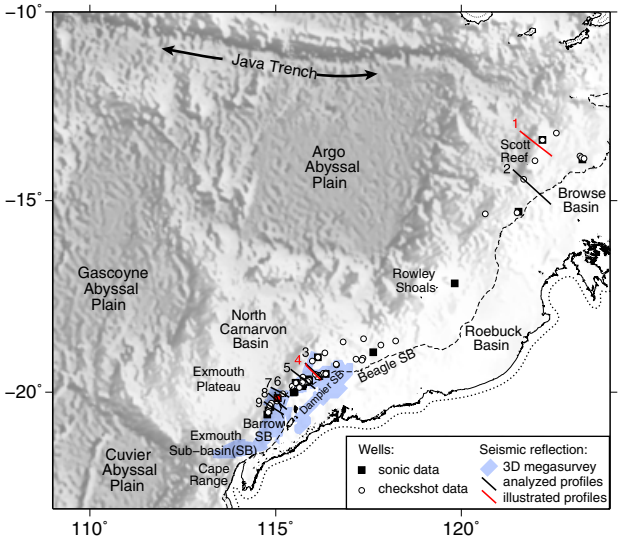


**Figure 8.** Shaded bathymetric map of Northwest Shelf (Figure 7). Open circles and solid squares = check shot and sonic data from wells which encountered Cenozoic carbonate rocks; red circle/square = check shot/sonic data from West Tryal Rocks 3 well; black dashed line = present day shelf break; black and red lines = two-dimensional seismic reflection profiles; blue polygons = location of Petroleum Geo-Services Carnarvon 3D MegaSurvey.

keeping pace with relative sea-level rise across the shelf (Figure 8). A comparison of drowned patch reefs, deposited near sea level, with contemporaneous clinoform rollovers in the northern Northwest Shelf shows that the depositional depth of clinoform rollovers matches paleobathymetric ranges determined by foraminiferal studies from the southern Northwest Shelf (e.g., Figures 10a and 10b).

[27] Sedimentary supply along the Northwest Shelf is predominantly controlled by in situ carbonate production, which is related to the depth of light penetration [*Pomar*, 2001]. The volume of carbonate sediment produced is controlled by sea-floor area above the carbonate production depth, favoring neritic heterozoan over photozoan biota [*Williams et al.*, 2011]. Accumulation of thick transgressive carbonate rocks over the last ~8 Ma is a direct consequence of progressive drowning of the continental shelf, which established neritic water depths and stimulated carbonate production over a wide shelf area. Rapid sedimentary production triggered destabilization of the present-day shelf, which is manifest by formation of shelf-normal submarine canyons and shelf-parallel normal faulting (Figure 11b). A belt of shelf-normal submarine canyons also formed during an earlier phase of aggradation. Canyon development waned and then re-intensified during the younger phase of aggradation (Figures 11a and 11c). This morphology is characteristic of high-stand carbonate shedding, as exemplified by the Bass Canyon off southeast Australia [*Schlager et al.*, 1994; *Mitchell et al.*, 2004; *Mitchell et al.*, 2007].

## 3.2. Stratal Analysis

[28] In order to quantify Neogene subsidence along the Northwest Shelf, we have analyzed the trajectory of the clinoform rollover position as a function of time. The trajectory of this paleobathymetrically constrained position is the clearest signal of relative sea-level change. It sidesteps large paleobathymetric uncertainties associated with conventional backstripping of wells at deep-water margins, whilst capturing a more complete stratigraphic record. First, the age of each clinoform rollover is determined. Second, seismic reflection images are converted from two-way travel time to depth. Third, the trajectory of rollover positions is decompacted and converted into a water load. Since the last rifting episode occurred several lithospheric time constants ago, the background gradient of Neogene post-rift subsidence is small and can be neglected.

[29] Our analysis concentrates on the North Carnarvon Basin where there is excellent three-dimensional seismic reflection data coverage calibrated by numerous boreholes with good Neogene biostratigraphy. This along shelf variation was assessed by analyzing two seismic profiles from the Browse Basin. Seismic reflection surveys were generously provided by Petroleum Geo-Services and by Geoscience Australia [*Fleming*, 2010]. Well completion reports with lithologies, check shot surveys, and sonic logs were sourced from the Geological Survey of Western Australia. Biostratigraphy was sourced from the Geoscience Australia Petroleum Wells database (http://dbforms.ga.gov.au/www/npm.well.search). Our results are supplemented by published interpretations of reflection seismic profiles (Figure 8) [*Young et al.*, 2001; *Hull and Griffiths*, 2002; *Cathro et al.*, 2003].

### 3.2.1. Age Constraints

[30] Ages of clinoform rollovers were constrained using microfossil zones tied to the geologic time scale [*Gradstein et al.*, 2004, Figure 9]. In the Barrow Sub-basin, the chronology of megasequence boundaries was established using the age range of biozones above and below each boundary. The age of each boundary was defined by the mean and range of ages from reliable wells

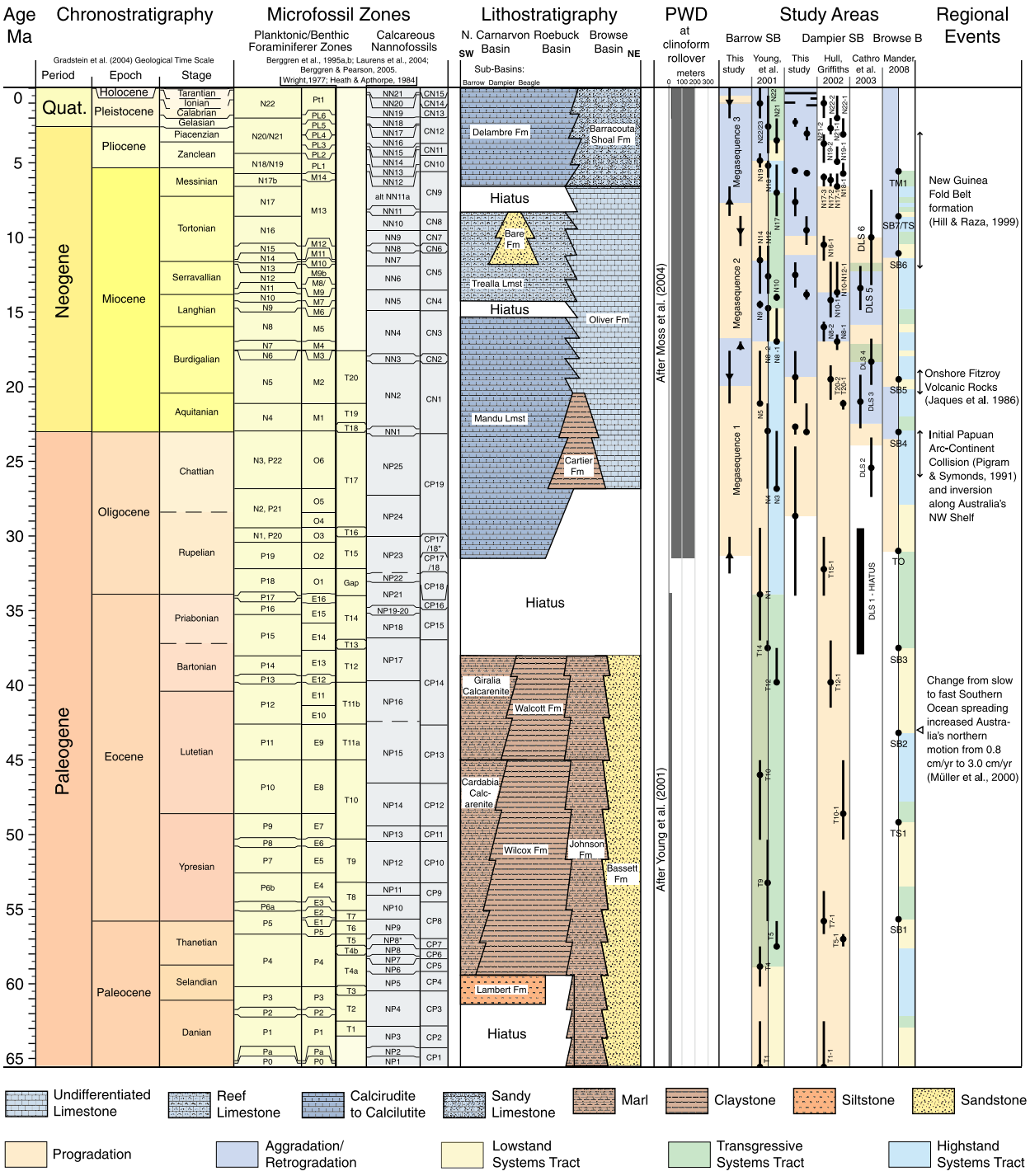


**Figure 9.** Cenozoic stratigraphy of Northwest Shelf using timescale of *Gradstein et al.* [2004]. In study areas on the right-hand side, vertical black lines with circles/triangles = biostratigraphic ranges used to construct subsidence curves (Figure 13); PWD = paleowater depth. Prepared using Time Scale Creator Pro (http://www.tscreator.org).

(Figure 9). Improved resolution and consistency of reflection horizons in the Dampier Sub-basin allowed us to date individual seismic reflections by direct ties with multiple wells within the three-dimensional seismic volume. In the Browse Basin, biozones reported by *Mander* [2008] and by *Longley et al.* [2002] were used. We used the same biozones to analyze published interpretations. When the age of an individual clinoform rollover could not be established directly, an age was assigned by linear interpolation between two known ages based on the distance along the clinoform trajectory.

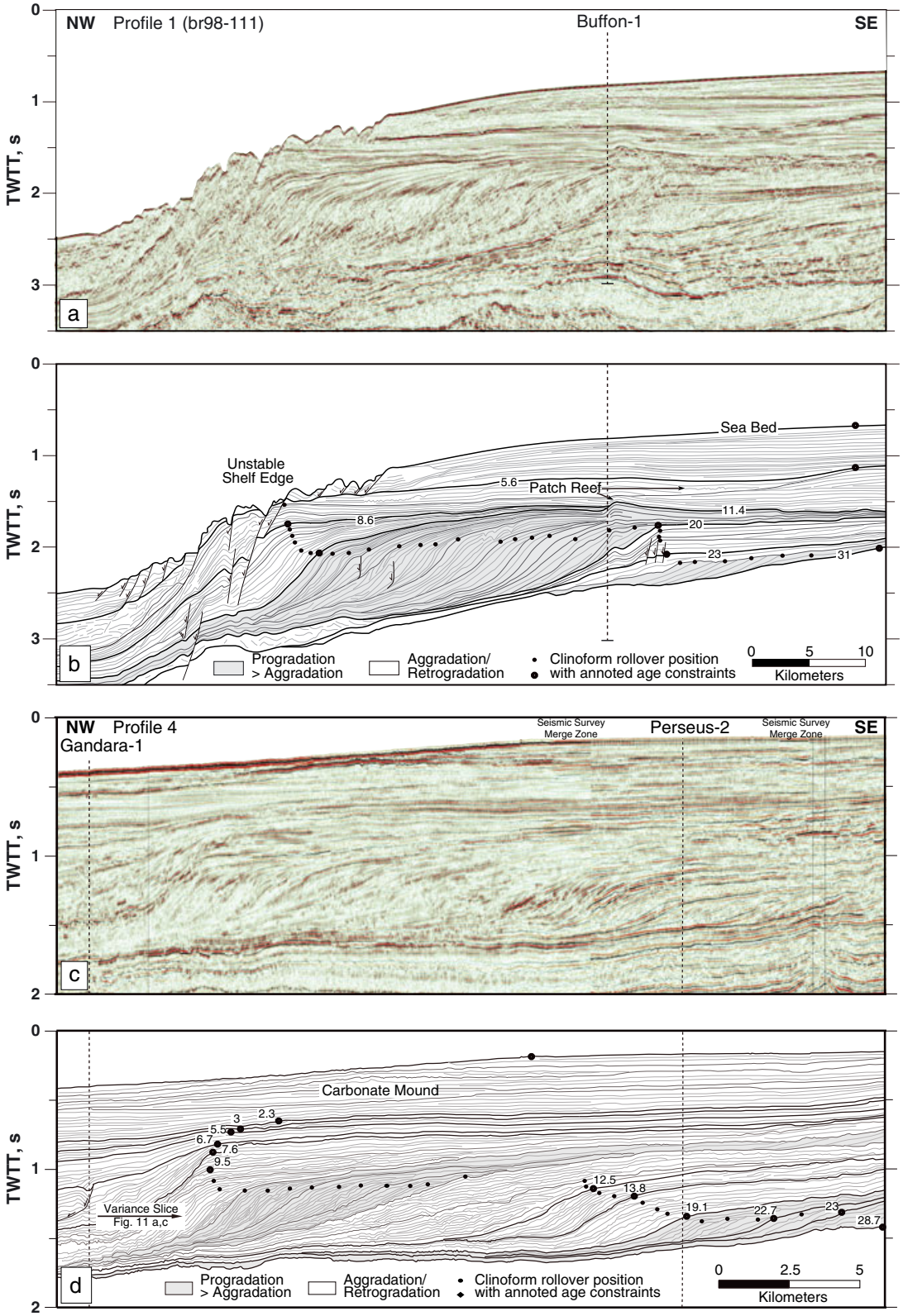


**Figure 10.** Seismic reflection profiles from Northwest Shelf (Figure 8). (a) and (b) Original and interpreted profile br98-111 with projected Buffon-1 well [*Fleming*, 2010]. Thick lines = dated horizons; thin lines = other horizons; vertical lines with arrows = normal faults; large circles = dated crests of clinoform rollovers; small circles = crests of clinoformal rollovers with interpolated ages (Figure 13h). (c) and (d) Original and interpreted profile taken from Petroleum Geo-Services Carnarvon 3D megasurvey which intersects Gandara-1 and Perseus-2 wells (Figure 13e). Annotation as before.

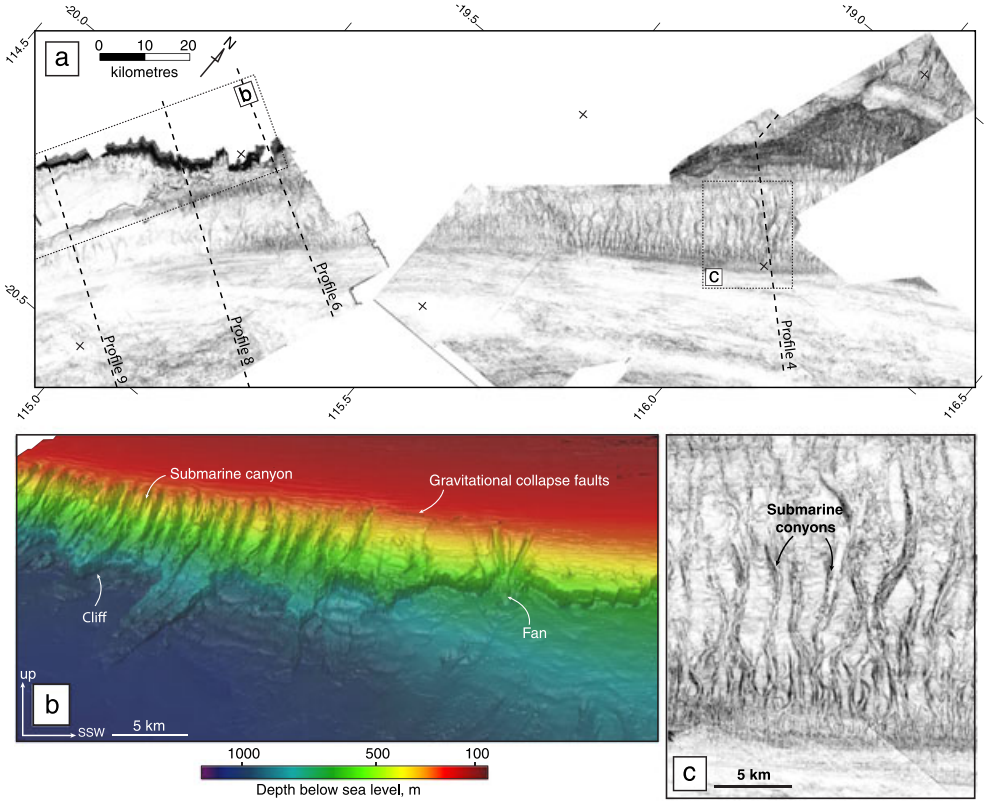


**Figure 11.** Seismic variance slices and three-dimensional perspective. (a) Horizontal variance slice at 1.34 s two-way travel time from PGS Carnarvon 3D megasurvey. Light and dark shading indicates greater and lesser degrees of coherence, respectively. Submarine canyons picked out by dark shading. Two phases of channelization, which correlate with periods of aggradation shown in Figure 10d, are visible over strike length of > 100 km. Insets show locations of Figures 11b and 11c. (b) Perspective view of seabed looking east and showing unstable shelf break with extensive channeling. (c) Close-up of older phase of submarine canyons.

### 3.2.2. Subsidence Analysis

[31] Depth conversion of the rollover position was carried out using a time-depth relationship based on compaction parameters (cf. section 2.2.2). Here $v_{sg}$ was increased to 6.53 km s$^{-1}$ to match a calcite mineralogy [*Christensen*, 1982]. Compaction parameters were estimated down to the base of clean carbonate rock for 56 wells with check shot surveys and/or sonic logs using equations (4) and (5). There is good agreement between compaction parameters estimated in different ways (e.g., West Tryal Rocks 3 well; Figure 12a–c). analyses are listed in the Supporting Information. The spatial variation of compaction parameters is summarized for different sub-basins in Figure 12d–12g. In each sub-basin, depth conversion was carried out, and the subsidence history was reconstructed using the mean and one standard deviation of $\phi_o$-$\lambda$ pairs (Table 2; Supporting Information). Each shelf-break position was back-stripped assuming a constant sea level following the method of *Sclater and Christie* [1980]. We assumed that the flexural rigidity of the lithosphere was negligible for long-wavelength loads since the elastic thickness of this margin is ~5 km [*Fowler and McKenzie*, 1989]. For the purposes of backstripping, we divided pre-Neogene strata into an upper unit, which comprised 70% carbonate and 30% shale, and a lower unit, which comprised 10% carbonate, 45% sandstone, and 45% shale. The thickness of the upper unit was calibrated by well logs, and the thickness of the lower unit was extended to 8 km, the minimum sediment thickness along the margin. Since this minimum is large, the deepest sedimentary rocks were fully compacted prior to Neogene sedimentation, which means that the exact thickness does not affect our results. However, failure to de-compact these pre-Neogene sedimentary rocks would introduce hundreds of meters of error.

### 3.2.3. Error Analysis

[32] There are three significant sources of error. First, and most importantly, the paleobathymetry of clinoform rollover positions is uncertain. We

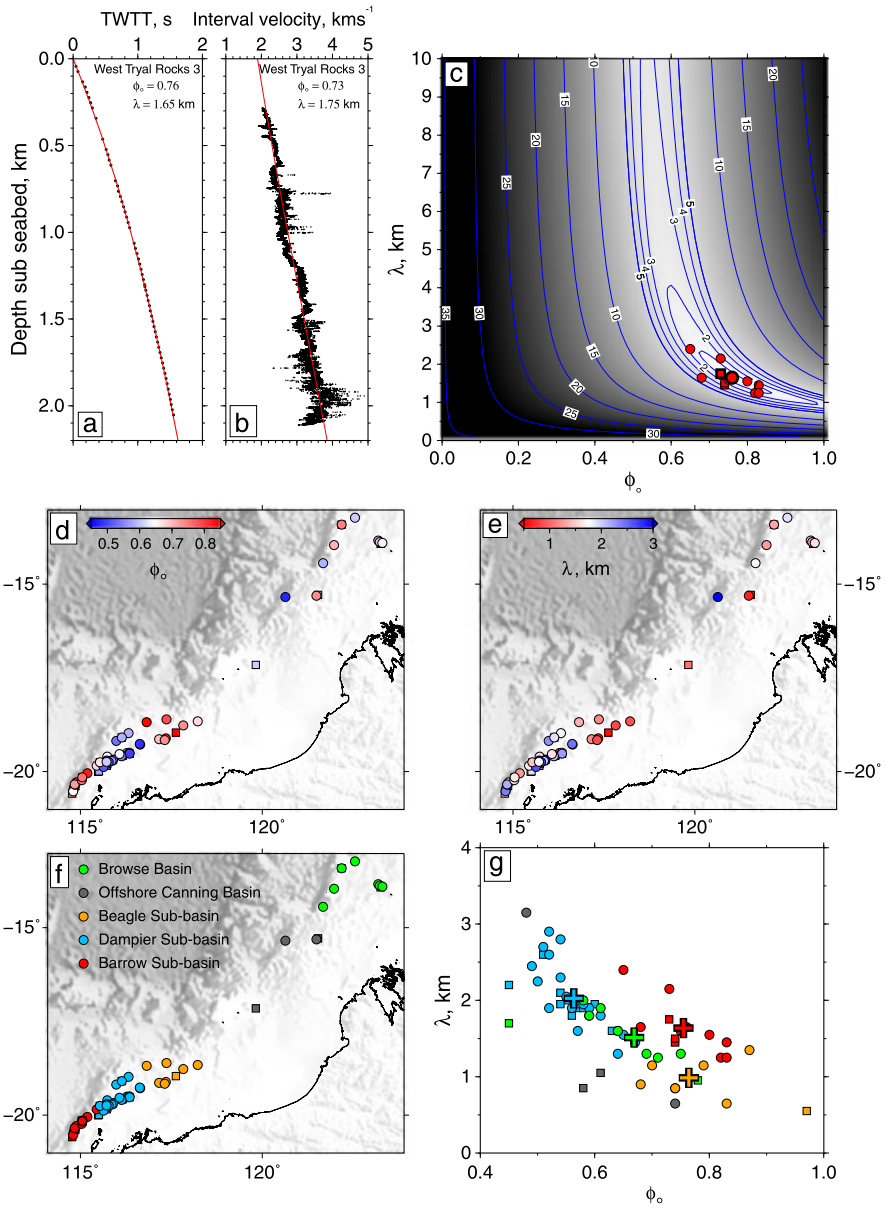


**Figure 12.** Compaction analyses of 56 wells intersecting Cenozoic platform carbonate rocks along Northwest Shelf. (a) Check shot survey for West Tryal Rocks 3 well (Figure 8). Solid circles = check shot measurements; red line = best-fit curve for given values of $\phi_\circ$ and $\lambda$. (b) Sonic log for West Tryal Rocks 3 well. Solid circles = log measurements; red line = best-fit curve for given values of $\phi_\circ$ and $\lambda$. (c) Contour map of residual misfit as function of $\phi_\circ$ and $\lambda$ obtained by fitting check shot data (equation (5)). Red circle/square outlined in black = values of $\phi_\circ$ and $\lambda$ at global minima for check shot/sonic data for West Tryal Rocks 3 well; other circles/squares = results for Barrow Sub-basin. (d) and (e) Maps of Northwest Shelf showing spatial distribution of $\phi_\circ$ and $\lambda$. Circles/squares = estimates derived from check shot/sonic data. (f) Map showing sub-basin grouping (Figure 8). (g) $\lambda$ as a function of $\phi_\circ$ for analyzed wells colored by sub-basin grouping. Crosses = mean values for each group (see Supporting Information for further details).

use a conservative estimate of ±90 m based on the benthic foraminifera analyses of *Cathro et al.* [2003] and of *Moss et al.* [2004]. Carbonate production rates for heterozoan oligophotic biota shows that growth rates can keep up with all but the most rapid rates of sea-level change [*Williams et al.*, 2011]. Furthermore, periodic erosion and thickening of clinoform topsets, related to changes in clinoform trajectory, suggest that clinoforms are sensitive to sea-level fluctuations on timescales of less than 0.5 Myr (Figure 10). Both observations imply that our water-depth estimate is an upper bound. Second, uncertainties in compaction parameters affect depth conversion, de-compaction, and unloading calculations. One standard variation

**Table 2.** Sediment Parameters

| Parameter | Solid Grain Density | Solid Grain Velocity | Initial Porosity | Compaction Decay Length |
|---|---|---|---|---|
| Symbol | $\rho_{sg}$ | $v_{sg}$ | $\phi_\circ$ | $\lambda$ |
| Units | Mg m$^{-3}$ | km s$^{-1}$ | Dimensionless | km |
| Oceanic sediment | $2.65 \pm 0.05$ | $5.5 \pm 0.5$ | Figure 3 | Figure 3 |
| Northwest Shelf carbonate[a] | 2.70 | 6.53 | Figure 12 | Figure 12 |
| Sandstone[b] | 2.65 | | 0.5 | 2.5 |
| Shale[b] | 2.70 | | 0.6 | 2.0 |
| Limestone[b] | 2.70 | | 0.4 | 1.0 |

[a]Solid grain parameters are for calcite from *Christensen* [1982].
[b]Parameters from *Sclater and Christie* [1980].

from the mean of compaction parameters has been propagated through these calculations, which show that the maximum subsidence error is ±55 m (Figure 13). Third, stratigraphic horizons can be dated to no better than ±1-3 Myr.

### 3.3. Results

[33] The biggest phase of subsidence is associated with a shelf-wide phase of stratal aggradation, which commenced at $8 \pm 2$ Ma (Figure 13, cf. Figure 10). The amplitude of this phase exceeds the paleobathymetric uncertainty and defines an amplitude gradient (200–300 m in the south, 500–650 m in the north). Figure 14a shows that its amplitude matches the residual bathymetry measured in the adjacent oceanic basin, which suggests a causal relationship. On several profiles, there is evidence for an earlier phase of rapid subsidence at $20 \pm 2$ Ma. Its amplitude is no more than 140 m which is within paleobathymetric error but suggestive of episodic drawdown.

[34] The maximum rate of drawdown is ~75 m Myr$^{-1}$ and occurs on the most northerly profile (Figure 8). This area is adjacent to Scott Reef, which is a large photozoan patch reef on this cool-water carbonate-dominated shelf. Whilst there is evidence for drowned patch reefs along this profile photozoan reefs must have a growth potential of at least ~75 m Myr$^{-1}$ since seismic imaging and drilling of Scott Reef indicate reef growth has matched subsidence since mid-Miocene times. After Stage 5e (125 ka), continuous subsidence has occurred at a rate of ~240 m Myr$^{-1}$ [*Collins and Testa*, 2010]. Subsidence of the Rowley Shoals and the Ningaloo Reef are consistent with a down-to-the-north subsidence gradient since Stage 5e, in agreement with our longer term rates. These observations challenge the notion that the $10^5$–$10^8$ year growth potential of reefs is ~40 m Myr$^{-1}$ [*Schlager*, 1999]. They also challenge the assertion that Miocene reef demise along the Marion Plateau, offshore northeast Australia, was caused by rapid drowning triggered by a combination of glacio-eustatic sea-level rise and dynamic drawdown at rates of 50–60 m Myr$^{-1}$ [*DiCaprio et al.*, 2010].

## 4. Epeirogeny of Australia

[35] We summarize Cenozoic epeirogenic observations from Australia's margin in a counter-clockwise circuit to elucidate the temporal evolution of residual topographic estimates from the oceanic realm (Figure 15; Supporting Information). We have omitted regions where crustal shortening has been documented (e.g., the Flinders Ranges, the Cape Range). We have supplemented our review with subsidence analyses from the Gippsland and Carpenteria Basins, where clinoformal topsets were penetrated by wells (Table 2; Supporting Information). These analyses place a minimum constraint on subsidence in these areas.

[36] In southwestern Australia, south of ~25°S, Late Eocene marine transgressive sedimentary rocks, which were originally deposited in near-shore paleovalleys now occur at elevations of up to 300 m as far as 400 km inland [*Haig and Mory*, 2003; *de Broekert and Sandiford*, 2005; *Hou et al.*, 2008; *De Silva and Smith*, 2010]. Along the west coast, Pliocene shorelines occur at elevations of up to 75 m with progressively younger shorelines at lower elevations [*Collins and Baxter*, 1984]. Geomorphological investigations of river profiles and cosmogenic dating of the Darling Escarpment suggest that it became emergent during Neogene times [*Jakica et al.*, 2011]. The sign and amplitude of oceanic residual topography along the west coast closely match the inferred uplift of this escarpment.

[37] Along the south coast, an array of paleoshorelines which crop out in the Eucla Basin, together with eastward migration of the basin's depocenter,

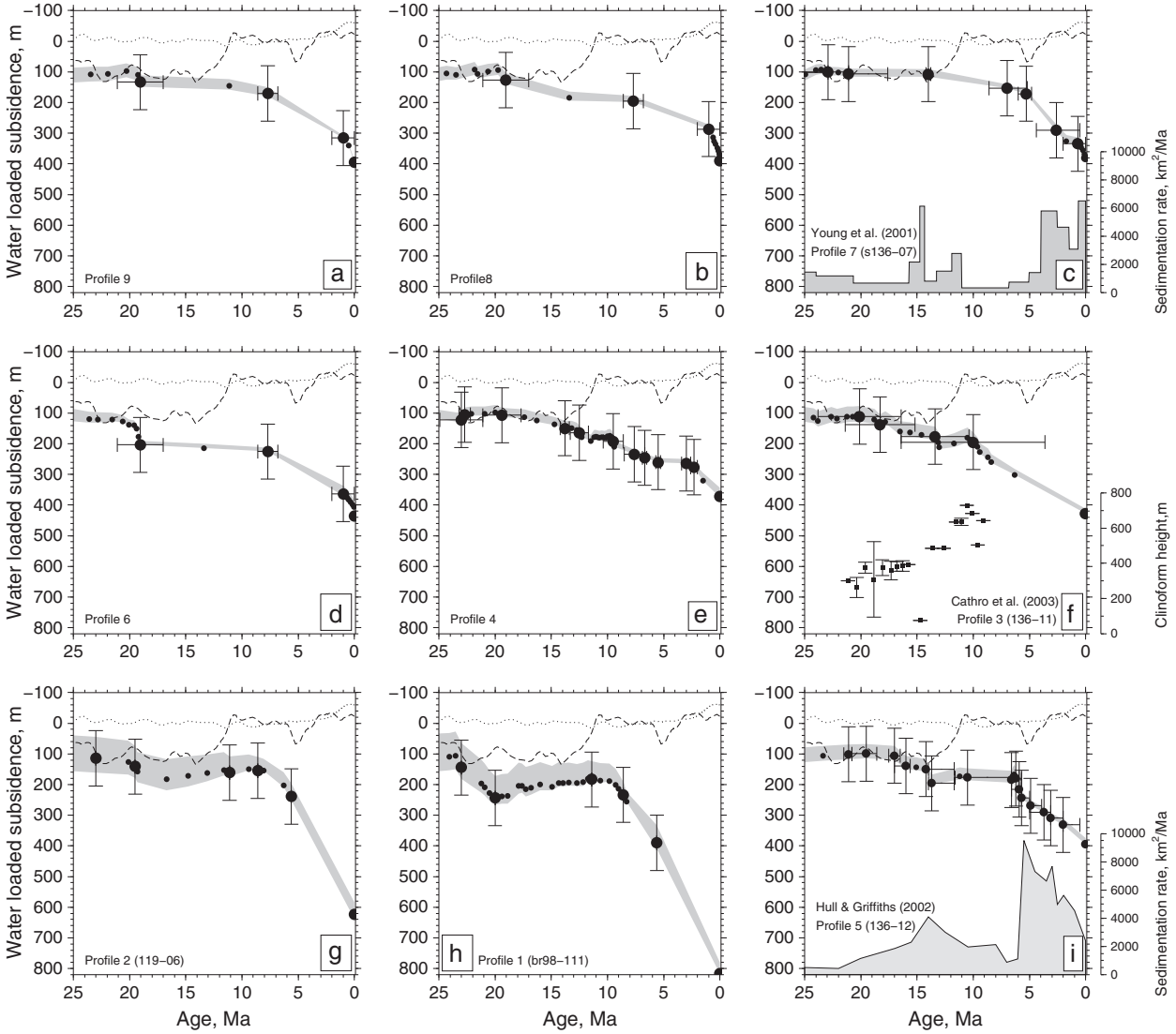


**Figure 13.** Water-loaded subsidence as function of time, starting at 25 Ma for clinoform rollover positions along Northwest Shelf (Figure 8). In each panel, location is given in bottom left-hand corner. Large solid circles with vertical/horizontal bars = dated estimates of water-loaded subsidence with paleobathymetric and chronological uncertainties; small solid circles = interpolated estimates of water-loaded subsidence; gray band = indication of uncertainty arising from $\phi_{\circ}$ and $\lambda$ estimates from each subbasin (Figure 12); dashed line = smoothed version of global eustatic sea level [*Haq et al*., 1987]; dotted line = smoothed version of global eustatic sea level [*Miller et al*., 2005]. In Figures 13c and 13i, gray histograms along *y* axis show undecompacted sedimentation rate as function of time. In Figure 13f, solid squares with vertical bars = undecompacted clinoform height.

indicates that this margin underwent regional differential, west-side up, emergence since mid-Eocene times [*Hou et al*., 2008]. In contrast to the west coast, the sign of oceanic residual depth does not match this history of emergence although there is a matching increase in drawdown amplitude from west to east. These apparently conflicting observations can be reconciled if the northward movement of the Australian plate is taken into account [*Sandiford*, 2007]. In other words, the plate is moving off a major convective downwelling, the Australian-Antarctic Discordance, and gradually emerging. This interpretation is consistent with the smooth gradient of residual topography and with the offshore stratigraphic architecture (Figure 15). Clinoformal topsets of prograding carbonate rocks are missing due to non-deposition or erosion. [*Feary and James*, 1998]. These observations disagree with water-loaded subsidence histories, which suggest that rapid anomalous drawdown occurred along the proximal shelf in the last 35 Myr. These histories imply that there is a change in sign of vertical motion at the coastline [*DiCaprio et al*., 2009; *Heine et al*., 2010]. The difficulties in

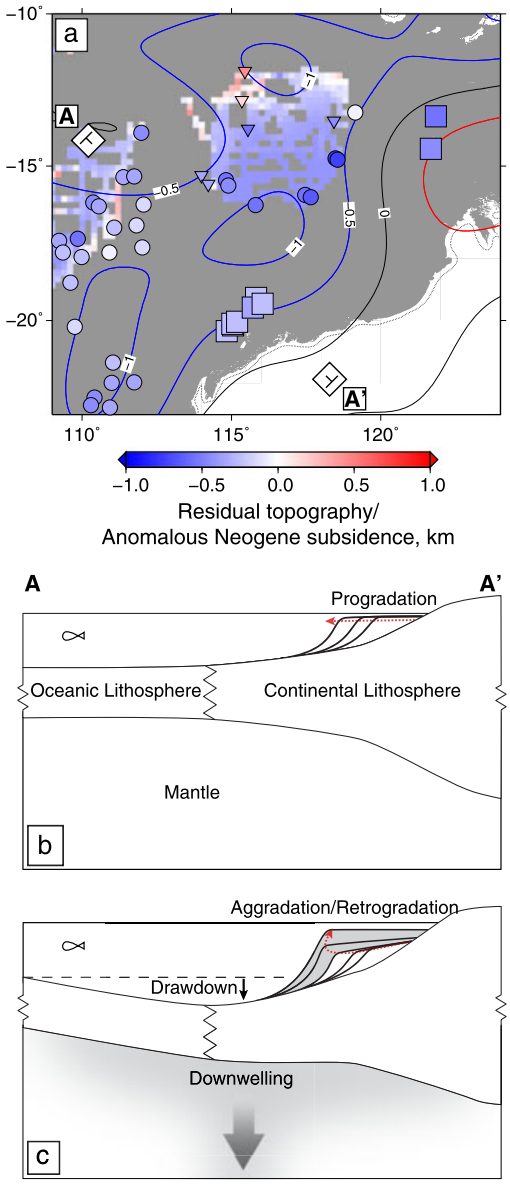


**Figure 14.** Anomalous Neogene subsidence on Northwest Shelf. (a) Comparison between oceanic and shelfal estimates of residual topography. Colored circles/lines = residual topography of oceanic floor (Figure 7); colored squares = anomalous Neogene subsidence (Figure 13); A-A′ shows location of cartoons in Figure 14b and 14c. (b) and (c) Cartoons showing how convective downwelling beneath the lithospheric plate causes transition from progradation to aggradation within carbonate platform.

assigning reliable paleobathymetries to the foresets and bottomsets of the prograding wedge suggest that the spatial gradient of vertical motion may not be significant.

[38] The biggest contrasts in oceanic residual topography and relative continental vertical motions are observed in southeast Australia. For example, along the southern coast, the most anomalously drawn-down oceanic lithosphere occurs between the Flinders and Otway Ranges. Immediately onshore in the Murray Basin, < 1 Ma strandlines occur at elevations of up to 175 m, yielding a maximum uplift rate of ~75 m $Myr^{-1}$ [*Wallace et al.*, 2005; *Sandiford et al.*, 2009]. Further east, between the Otway Ranges and the Gippsland Basin, hundreds of meters of uplift have been inferred from the existence of a Miocene-Pliocene (5–10 Ma) unconformity [*Dickinson et al.*, 2002]. A down-to-the-north gradient in oceanic residual topography (+300 m to −200 m) occurs between Tasmania and the main land. Water-loaded histories determined for wells in the southern Gippsland Basin suggest that anomalous subsidence occurred since Late Eocene times (Supporting Information). Immediately onshore, palynological assemblages from Eocene paleochannels preserved at ~1700 m on Mount Hotham suggest that they were deposited on a coastal plain which implies that the Eastern Highlands were uplifted by > 1 km during the Cenozoic Era [*Holdgate et al.*, 2008].

[39] In northeast Australia, water-loaded subsidence histories show that an anomalous subsidence event commenced at ~6–11 Ma [*Müller et al.*, 2000b; *DiCaprio et al.*, 2010]. The amplitude of this event is consistent with drawdown observed in the Coral and northern Tasman Seas (Figure 15). Finally, the Duyken-1 well from the Carpenteria Basin shows that an anomalous subsidence event commenced at ~12 Ma. Thus, the amplitude and gradient of oceanic residual topography is consistent with near synchronous anomalous subsidence over a region, which stretches from the Northwest Shelf to the northeast coast of Australia and supports the notion that this drawdown is a long-wavelength feature.

## 5. Discussion

[40] An anomalous and largely synchronous subsidence event has affected the northern portion of Australia and its surrounding oceanic basins. This event developed within the last 9 ± 3 Ma, and its amplitude often exceeds several hundred meters. Neither its size, its timing, nor its spatial distribution can be explained by a glacio-eustatic rise in sea level [*Haq et al.*, 1987; *Miller et al.*, 2005]. Instead, we propose that rapid subsidence is caused by convective downwelling within the upper mantle. A significant corollary is that the sequence stratigraphic and geomorphic architecture of the extensive carbonate platform which rims the Northwest Shelf indirectly records useful, and otherwise unattainable, information about the fluid dynamics of deep Earth processes.

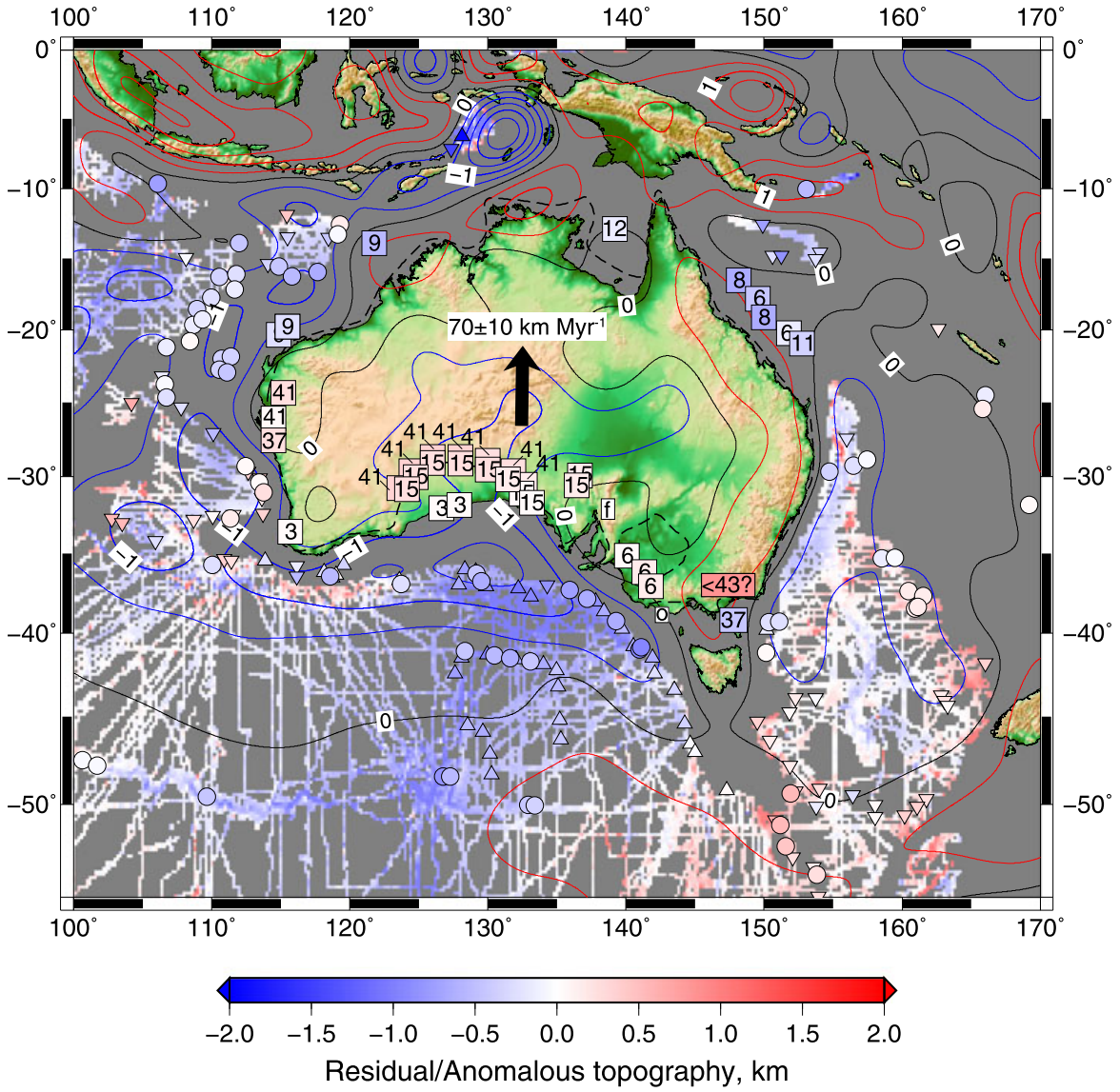


**Figure 15.** Summary map which shows spatial and temporal variation of residual topography. Colored circles/triangles binned in 2° × 2° cells (cf. Figure 7); colored lines = selected ship-track data; colored squares with numbers = relative epeirogenic movement (color = magnitude of movement, number = onset age in Ma); colored contours = dynamic topography estimated from long-wavelength gravity anomalies (see Figure 7); black dashed line = 15 Ma paleoshoreline of *Sandiford* [2007]; black arrow = average vector of Australian Plate for last 5.8 Ma with respect to HS3-NUVEL-1A hotspot reference frame of *Gripp and Gordon* [2002]; f = Flinders Ranges, o = Otway Ranges.

[41] Following *Sandiford* [2007], we suggest that Neogene emergence of Australia's southern margin can also be accounted for by convective processes. Here the spatial pattern of dynamic topography suggests that the post-Eocene record of emergence is caused by northward translation of Australia off the dynamic topography low of the Australian-Antarctic Discordance (Figure 15). The pattern of dynamic topography is consistent with a negative long-wavelength free-air gravity anomaly and with anomalously fast upper mantle shear wave velocities (Figure 6). There are also significant gradients in dynamic topography across the east coast of Australia possibly associated with the eastern Australian hotspot [*Wellman and McDougall*, 1974]. This inference is supported by onshore positive long-wavelength free-air gravity anomalies, indicative of dynamic support, and offshore negative gravity anomalies (Figure 15).

[42] We have selected six locations where the history of dynamic topography can be investigated in more detail and compared with predictive models (Figure 16). At each location, upper and lower bounds of dynamic topography as a function of time

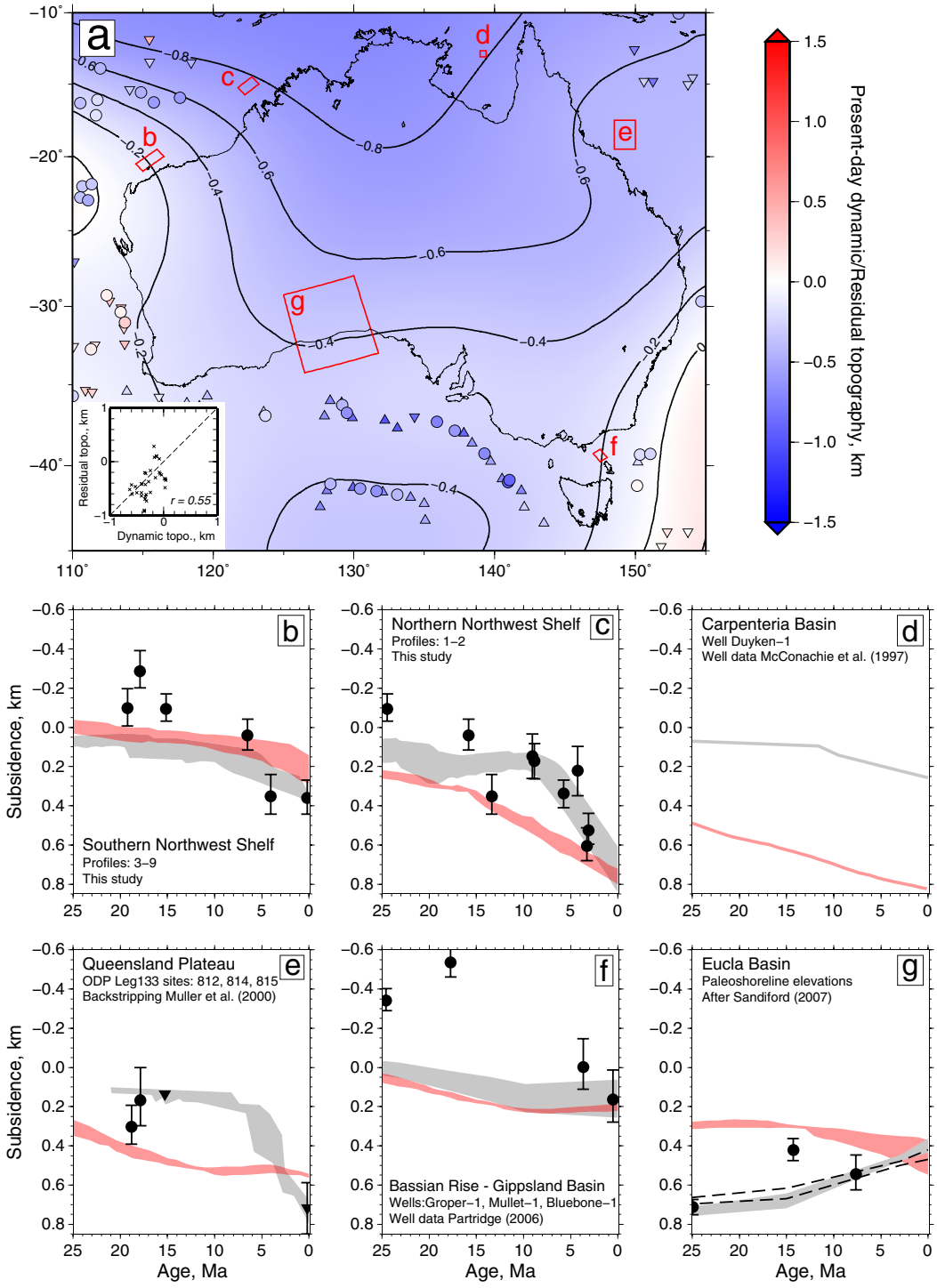


**Figure 16.** Comparison of observed and predicted dynamic topography allowing for plate translation. (a) Predicted present-day dynamic topography from *Heine et al.* [2010] who scaled their results by 0.55. Numbered contours and red-blue shading = water-loaded version of predicted dynamic topography; colored circles/triangles = observed estimates of residual topography from our study binned in 2°×2° cells; lettered boxes = locations of Figures 16b–16g; inset = residual topography plotted against predicted dynamic topography with dashed line at 45°. (b)–(g) Gray bands = water-loaded subsidence/uplift as function of time based on combination of clinoform rollover trajectories, wells, and paleoshorelines. Present-day values are pinned to nearest value of oceanic residual topography apart from isolated Figure 16d. In Figure 16g, dashed lines = range of air-loaded uplift. Solid circles with vertical bars = projected residual topography as function of time obtained by translating Australian Plate across spatial pattern of residual topography (Figure 15). Pink bands = predicted dynamic topography calculated by *Heine et al.* [2010]. See also Supporting Information.

have been calculated from subsidence or uplift histories. Present-day values are normalized with respect to the closest estimate of oceanic residual topography. In most places, dynamic topography appears to have grown during the last 25 Myr from the reference level (i.e., a level unperturbed by dynamic topography). One exception is the Euclas Basin, which strongly supports the notion that the southern margin is emerging from a region of convective drawdown. These observations challenge the hypothesis that Neogene epeirogeny of Australia is caused by drifting from a dynamic swell toward a dynamic trough [*DiCaprio et al*., 2009].

[43] An important complication is that the Australian Plate is translating northward at 60–80 mm $yr^{-1}$ in the hotspot reference frame [*Gripp and Gordon*, 2002]. Is the spatial and temporal pattern of dynamic topography a consequence of the Australian Plate overriding a stable downwelling zone within the convecting mantle? Alternatively, does this pattern reflect time-dependent convection? It has been suggested that Australia's northward translation toward a major putative drawdown centered in Southeast Asia triggered regional subsidence, which progressively swept southward across the plate [*Lithgow-Bertelloni and Gurnis*, 1997; *Sandiford*, 2007; *Sandiford et al*., 2009; DiCaprio et al., 2009]. Thus, one end-member model is that in which the Australian Plate gradually tilts toward the northeast about a roughly northwest striking axis. If so, we expect that the 15 Ma history of emergence recorded by paleocoastlines along the southern margin be mirrored by coeval subsidence on the northern margin. Instead, our observations show that the epeirogeny of Australia varies on shorter spatial and temporal scales and cannot easily be accounted for by dipping plane approximations. A puzzling complication is that along the Northwest Shelf, synchronous drawdown commenced at $8 \pm 2$ Ma and may extend around the northern coast to the Coral Sea. This synchroneity implies that convective downwelling developed recently and tracks the plate, provided the mantle boundary beneath Australia has an approximately east-west strike.

[44] The idea that the Australian Plate is drifting over a stationary convective downwelling can be investigated by assuming that the Australian Plate has translated across a fixed spatial distribution of dynamic topography. At different locations, the history of vertical motions caused by plate translation can then be compared with observations. In Figure 16, we show the histories for six locations, which were determined by projecting the nearest $4° \times 4°$ cell averages of oceanic residual floor depths onto a north-south trajectory. Distance was converted into geologic time by assuming that the Australian Plate translates northward at 70 mm $yr^{-1}$. The predicted and observed subsidence trajectories are broadly consistent which suggests that epeirogeny of the Australian Plate is primarily influenced by translation over a large, quasi-stationary downwelling. For example, along the length of the Northwest Shelf, subsidence during the last 25 Myr is consistent with plate translation, although we suspect that shorter wavelength convective features play a role in generating the observed scatter (Figures 16b and 16c). Subsidence of the Queensland Plateau and emergence of the Eucla Basin can be explained in a similar way. The largest disagreement occurs in southeast Australia where there are significant spatial gradients of dynamic topography at an acute angle with respect to plate translation. Convective circulation of the mantle undoubtedly has a range of periodicities. Given the large velocity of the Australian Plate, we think that it is reasonable that long-wavelength convective downwelling is effectively stationary over the last 25 Myr but that short wavelength convective anomalies, which grow and decay on smaller timescales, moderate the temporal pattern of dynamic topography. In order to account for the synchroneity of subsidence across northern Australia, we infer the presence of highly non-linear mantle boundaries beneath Australia, a feature reflected in the tomography but considerably different to first-order gradients within the geoid.

[45] Finally, our detailed observations can be used to test predictive models. For example, *Heine et al*. [2010] have calculated the spatial and temporal variation of dynamic topography by running the advective component of a convective simulation backward through time. Their starting point for this simulation is a mantle density distribution which is based upon the S20RTS seismic tomographic model of *Ritsema et al*. [1999]. Translation of the Australian Plate is also taken into account. A simulation for the Cenozoic Era was matched with the dynamic topographic observations of *DiCaprio et al.* [2009] by varying an empirical scaling factor. In Figure 16, we compare predictions based on this simulation with our observations. In most locations, there is a good match between the predicted and observed dynamic topography at the present day. An important exception is the Perth abyssal plain where *Heine et al*. [2010] predict a present-day value of −150 m, whereas we obtained a value of about +150 m. Over the last 25 Myr, however, there are significant mismatches along the northern portion of the Northwest Shelf, along the Queensland Plateau, and for the Eucla Basin.

## 6. Conclusions

[46] We have described and analyzed the spatial and temporal pattern of dynamic topography for a region encompassing Australia. The cornerstone of our study is an analysis of residual bathymetry of oceanic lithosphere which abuts the continental shelf. This analysis exploits a combined database of ~200 seismic reflection and wide-angle experiments, which enabled us to make accurate measurements of water-loaded subsidence as a function of plate age. By removing the effects of the well-known age-depth relationship, we have isolated residual bathymetric anomalies. It is likely that these anomalies were generated by changes in convective circulation beneath the oceanic plate. Our study yielded 282 spot measurements averaged into 1° bins. These measurements were supplemented with bathymetric profiles which were carefully cropped to exclude oceanic plateaux and regions blanketed by thick sediment. Along the Northwest Shelf, we have analyzed the Neogene subsidence history using calibrated two- and three-dimensional seismic surveys. Our results show that a rapid, anomalous subsidence event commenced at 9 ± 3 Ma and continued to the present day at rates of up to 75 m $Myr^{-1}$. This widespread event cannot be accounted for by glacio-eustatic sea-level rise. Instead, we propose that it was generated by convective downwelling within the mantle.

[47] We have also collated other marine and terrestrial observations, which have been attributed to changes in the pattern of dynamic topography. A regional synthesis is then used to show that the spatial and temporal variation of dynamic topography can be largely attributed to rapid northward translation of the Australian Plate. However, there are notable discrepancies, which suggest that short wavelength dynamic topographic anomalies grow and decay as the plate moves northward.

[48] We suggest that careful studies of the subsidence records of ancient oceanic lithosphere can yield useful information about spatial patterns of dynamic topography. Since these records abut continental margins, the temporal evolution of these patterns can be established by analyzing the stratigraphic architecture of carbonate and siliciclastic deposits. Our results imply that second- and third-order sequence stratigraphic cycles may be explained by changes in convective circulation beneath the lithosphere. We hope that our database will be used to refine models which predict the evolution of dynamic topography on Earth.

## Acknowledgments

[49] KC is supported by Geosciences Australia. We are grateful to Petroleum Geo-Services for generously providing access to three-dimensional seismic reflection data. A. Fleming and M. Tully helped to collate legacy seismic surveys, and the Geological Survey of Western Australia provided well data. We thank R. Blewett, R. Hackney, I. Frame, D. Lyness, G. Roberts, and N. Pocock for their help. N. Flament and S. Gallagher wrote helpful reviews. Most figures were prepared using the Generic Mapping Tools program of Wessel and Smith [1998]. KC publishes with permission of the CEO of Geoscience Australia. Geocat number 74286; Earth Sciences Contribution Number esc.2638.

## References

Athy, L. F. (1930), Density, porosity, and compaction of sedimentary rocks, *AAPG Bull.*, *14*(1), 1–24.

Berggren, W. A., and P. N. Pearson (2005), A revised tropical to subtropical Paleogene planktonic foraminiferal zonation, *J. Foramin. Res.*, *35*(4), 279–298, doi:10.2113/35.4.279.

Berggren, W. A., F. J. Hilgen, C. G. Langereis, D. V. Kent, J. D. Obradovich, I. Raffi, M. E. Raymo, and N. J. Shackleton (1995a), Late Neogene chronology: New perspectives in high-resolution stratigraphy, *Geol. Soc. Am. Bull.*, *107*(11), 1272–1287, doi:10.1130/0016-7606(1995)107<1272:lncnpi>2.3.co;2.

Berggren, W. A., D. V. Kent, I. Swisher, C. C., and M.-P. Aubry (1995b), A revised Cenozoic geochronology and chronostratigraphy, in *Geochronology, Time Scales and Global Stratigraphic Correlations: A Unified Temporal Framework for a Historical Geology*, Society of Economic Paleontologists and Mineralogists Special Publication, vol. *54*, edited by W. A. Berggren, D. V. Kent, H. P. Aubry, and J. Hardenbol, pp. 129–212, SEPM Special Publication, Tulsa.

Bry, M., and N. White (2007), Reappraising elastic thickness variation at oceanic trenches, *J. Geophys. Res.*, *112*(B8), B08414, 10.1029/2005JB004190.

Burke, K. (1996), The African Plate, *S. Afr. J. Geol.*, *99*(4), 341–409.

Carlson, R. L., and C. N. Herrick (1990), Densities and porosities in the oceanic crust and their variations with depth and age, *J. Geophys. Res.*, *95*(B6), 9153–9170.

Cathro, D. L., and G. D. Karner (2006), Cretaceous-Tertiary inversion history of the Dampier Sub-basin, northwest Australia: Insights from quantitative basin modelling, *Mar. Petrol. Geol.*, *23*(4), 503–526, doi:10.1016/j.marpetgeo.2006.02.005.

Cathro, D. L., J. Austin, James A., and G. D. Moss (2003), Progradation along a deeply submerged Oligocene-Miocene heterozoan carbonate shelf: How sensitive are clinoforms to sea level variations?, *AAPG Bull.*, *87*(10), 1547–1574, doi:10.1306/05210300177.

Cazenave, A., A. Souriau, and K. Dominh (1989), Global coupling of earth surface topography with hotspots, geoid and mantle heterogeneities, *Nature*, *340*(6228), 54–57, doi:10.1038/340054a0.

Christensen, N. I. (1982), Seismic velocities, in *Handbook of Physical Properties of Rocks, vol. II*, edited by R. S. Carmichael, pp. 57–74, CRC Press, Boca Raton, Fla.

Colin, P., and L. Fleitout (1990), Topography of the ocean-floor—Thermal evolution of the lithosphere and interaction of deep mantle heterogeneities with the lithosphere, *Geophys. Res. Lett.*, *17*(11), 1961–1964, doi:10.1029/GL017i011p01961.

Collins, L. B., and J. L. Baxter (1984), Heavy mineral-bearing strandline deposits associated with high-energy beach environments, southern Perth Basin, Western Australia, *Aust. J. Earth Sci.*, *31*(3), 287–292, doi:10.1080/14400958408527931.

Collins, L. B., and V. Testa (2010), Quaternary development of resilient reefs on the subsiding Kimberley continental margin, northwest Australia, *Braz. J. Oceanogr.*, *58*, 67–77, doi:10.1590/S1679-87592010000500007.

Crosby, A. G., and D. McKenzie (2009), An analysis of young ocean depth, gravity and global residual topography, *Geophys. J. Int.*, *178*(3), 1198–1219, 10.1111/j.1365-246X.2009.04224.x.

Crosby, A. G., D. McKenzie, and J. G. Sclater (2006), The relationship between depth, age and gravity in the oceans, *Geophys. J. Int.*, *166*(2), 553–573, doi:10.1111/j.1365-246X.2006.03015.x.

Crosby, A. G., N. J. White, G. R. H. Edwards, M. Thompson, R. Corfield, and L. Mackay (2011), Evolution of deep-water rifted margins: Testing depth-dependent extensional models, *Tectonics*, *30*, TC1004, doi:10.1029/2010TC002687.

Crough, S. T. (1983), The correction for sediment loading on the seafloor, *J. Geophys. Res.*, *88*(Nb8), 6449–6454, doi:10.1029/JB088iB08p06449.

de Broekert, P., and M. Sandiford (2005), Buried inset-valleys in the eastern Yilgarn Craton, Western Australia: Geomorphology, age, and allogenic control, *J. Geol.*, *113*(4), 471–493, doi:10.1086/430244.

De Silva, J., and R. A. Smith (2010), Significance of paleovalley sediments and landscape in the development of stream salinity in three southwest Australian catchments, *Aust. J. Earth Sci.*, *57*(2), 221–230, doi:10.1080/08120090903521689.

DiCaprio, L., M. Gurnis, and R. D. Müller (2009), Long-wavelength tilting of the Australian continent since the late Cretaceous, *Earth Planet. Sci. Lett.*, *278*(3-4), 175–185, doi:10.1016/j.epsl.2008.11.030.

DiCaprio, L., R. D. Müller, and M. Gurnis (2010), A dynamic process for drowning carbonate reefs on the northeastern Australian margin, *Geology*, *38*(1), 11–14, doi:10.1130/G30217.1.

Dickinson, J. A., M. W. Wallace, G. R. Holdgate, G. R. Gallagher and L. Thomas (2002), Origin and timing of the Miocene-Pliocene unconformity in southeast Australia, *J. Sed. Res.*, *72*(2), 317–332, doi:10.1306/082701720288.

Divins, D. (2008), NGDC total sediment thickness of the world's oceans and marginal seas. http://www.ngdc.noaa.gov/mgg/sedthick/sedthick.html.

Feary, D. A., and N. P. James (1998), Seismic stratigraphy and geological evolution of the Cenozoic, cool-water Eucla platform, Great Australian Bight, *AAPG Bull.*, *82* (5A), 792–816.

Fleming, A. (2010), 2010 Geoscience Australia acreage release data package. http://www.ga.gov.au/energy/projects/acreage-release-and-promotion.html.

Fowler, S., and D. McKenzie (1989), Gravity studies of the Rockall and Exmouth Plateaux using SEASAT altimetry, *Basin Res.*, *2*(1), 27–34, 10.1111/j.1365-2117.1989.tb00024.x.

Goncharov, A. (2004), Basement and crustal structure of the Bonaparte and Browse Basins, Australian northwest margin, in *Timor Sea Petroleum Geoscience. Proceedings of the Timor Sea Symposium, Darwin*, edited by G. Ellis, P. Baillie, and T. Munson, pp. 551–566, Northern Territory Geological Survey, Special Publication 1.

Gradstein, F. M., J. G. Ogg, and A. G. Smith (2004), *A Geologic Time Scale 2004*, Cambridge University Press, Cambridge.

Gripp, A. E., and R. G. Gordon (2002), Young tracks of hotspots and current plate velocities, *Geophys. J. Int.*, *150* (2), 321–361, doi:10.1046/j.1365-246X.2002.01627.x.

Gurnis, M., R. D. Müller, and L. Moresi (1998), Cretaceous vertical motion of Australia and the Australian-Antarctic discordance, *Science*, *279*(5356), 1499–1504, doi:10.1126/science.279.5356.1499.

Hager, B. H. (1984), Subducted slabs and the geoid: Constraints on mantle rheology and flow, *J. Geophys. Res.*, *89*(B7), 6003–6015, doi:10.1029/JB089iB07p06003.

Hager, B. H., and M. A. Richards (1989), Long-wavelength variations in Earth's geoid: Physical models and dynamical implications, *Philos. T. Roy. Soc. A*, *328*(1599), 309–327, doi:10.1098/rsta.1989.0038.

Haig, D. W., and A. J. Mory (2003), New record of siliceous, marine, late Eocene from Kalbarri, Western Australia, *J. R. Soc. W. Aust.*, *86*, 107–113.

Haq, B. U., J. Hardenbol, and P. R. Vail (1987), Chronology of fluctuating sea levels since the Triassic, *Science*, *235*(4793), 1156–1167, doi:10.1126/science.235.4793.1156.

Heath, R., and M. C. Apthorpe (1984), New formation names for the Late Cretaceous and Tertiary sequence of the southern Northwest Shelf, *Geological Survey Western Australia Record*, *7*, 1–35.

Heine, C., and R. D. Müller (2005), Late Jurassic rifting along the Australian North West Shelf: Margin geometry and spreading ridge configuration, *Aust. J. Earth Sci.*, *52*(1), 27–39, doi:10.1080/08120090500100077.

Heine, C., R. D. Müller, B. Steinberger, and L. DiCaprio (2010), Integrating deep earth dynamics in paleogeographic reconstructions of Australia, *Tectonophysics*, *483*(1-2), 135–150, doi:10.1016/j.tecto.2009.08.028.

Hill, K. C., and A. Raza (1999), Arc-continent collision in Papua Guinea: Constraints from fission track thermochronology, *Tectonics*, *18*(6), 950–966, doi:10.1029/1999TC900043.

Hillis, R. R., M. Sandiford, S. D. Reynolds, and M. C. Quigley (2008), Present-day stresses, seismicity and Neogene-to-recent tectonics of Australia's passive margins: Intraplate deformation controlled by plate boundary forces, *Geol. Soc., Lon., Spec. Pub.*, *306*(1), 71–90, doi:10.1144/sp306.3.

Holdgate, G. R., M. W. Wallace, S. J. Gallagher, B. E. Wagstaff, and D. Moore (2008), No mountains to snow on: Major post-Eocene uplift of the east Victoria highlands; evidence from Cenozoic deposits, *Aust. J. Earth Sci.*, *55*, 211–234, doi:10.1080/08120090701689373.

Holmes, R. C., M. Tolstoy, J. R. Cochran, and J. S. Floyd (2008), Crustal thickness variations along the Southeast Indian Ridge (100 116 E) from 2-D body wave tomography, *Geochem. Geophys. Geosyst.*, *9*, Q12020, 10.1029/2008GC002152.

Hou, B., L. A. Frakes, M. Sandiford, L. Worrall, J. Keeling, and N. F. Alley (2008), Cenozoic Eucla Basin and associated palaeovalleys, southern Australia—Climatic and tectonic influences on landscape evolution, sedimentation and heavy mineral accumulation, *Sed. Geol.*, *203*(1–2), 112–130, doi:10.1016/j.sedgeo.2007.11.005.

Hull, J., and C. Griffiths (2002), Sequence stratigraphic evolution of the Albian to recent section of the Dampier Sub-basin, North West Shelf Australia, in *The Sedimentary Basins of Western Australia 3: Proc. Pet. Exp. Soc. Aust. Sym*, edited by M. Keep and S. Moss, pp. 617–639, PESA, Perth, WA.

Jakica, S., M. C. Quigley, M. Sandiford, D. Clark, L. K. Fifield, and A. Alimanovic (2011), Geomorphic and cosmogenic nuclide constraints on escarpment evolution in an intraplate setting, Darling Escarpment, Western Australia, *Earth Surface Processes and Landforms*, *36*(4), 449–459, doi:10.1002/esp.2058.

Jaques, A. L., J. D. Lewis, and C. B. Smith (1986), The Kimberlites and Lamproites of Western Australia, *Geological Survey of Western Australia Bulletin*, *132*, 168 p.

Kaban, M. K., P. Schwintzer, I. M. Artemieva, and W. D. Mooney (2003), Density of the continental roots:

Compositional and thermal contributions, *Earth Planet. Sci. Lett.*, *209*(1-2), 53–69, doi:10.1016/S0012-821x(03)00072-4.

Keep, M., C. M. Powell, and P. Baillie (1998), Neogene deformation of the north west shelf, in *The Sedimentary Basins of Western Australia 2: Proceedings of West Australian Basins Symposium (WABS2)*, Perth, Western Australia, edited by P. G. Purcell and R. R. Purcell, pp. 81–91, PESA, Perth.

Kennard, J., I. Deighton, D. Ryan, D. Edwards, and C. Boreham (2003), Subsidence and thermal history modelling: New insights into hydrocarbon expulsion from multiple petroleum systems in the Browse Basin, in *Timor Sea Petroleum Geoscience. Proceedings of the Timor Sea Symposium, Darwin*, 19–20 June 2003, vol. *1*, edited by G. Ellis, P. Baillie, and T. Munson, pp. 411–435, Northern Territory Geological Survey, Spec. Pub: Darwin.

Lithgow-Bertelloni, C., and M. Gurnis (1997), Cenozoic subsidence and uplift of continents from time-varying dynamic topography, *Geology*, *25*(8), 735–738.

Longley, I. M., et al. (2002), The North West Shelf of Australia—A Woodside perspective, in The Sedimentary Basins of Western Australia 3: Proc. Pet. Exp. Soc. Aust. Sym, edited by M. Keep and S. Moss, pp. 27–88, PESA, Perth.

Louden, K. E., B. E. Tucholke, and G. N. Oakey (2004), Regional anomalies of sediment thickness, basement depth and isostatic crustal thickness in the North Atlantic Ocean, *Earth Planet. Sci. Lett.*, *224*(1-2), 193–211, doi:10.1016/j.epsl.2004.05.002.

Lourens, L., F. Hilgen, N. J. Shackleton, J. Laskar, and D. Wilson (2004), The Neogene period, in A Geologic Time Scale 2004, edited by F. M. Gradstein, J. G. Ogg, and A. G. Smith, pp. 409–440, Cambridge Uni. Press, Cambridge.

Mander, J. (2008), Cainozoic platform evolution, Browse Basin, North-West Shelf, Western Australia, Hon. Thesis, Uni. W. Aust.

Miller, K. G., M. A. Kominz, J. V. Browning, J. D. Wright, G. S. Mountain, M. E. Katz, P. J. Sugarman, B. S. Cramer, N. Christie-Blick, and S. F. Pekar (2005), The Phanerozoic record of global sea-level change, *Science*, *310*(5752), 1293–8, doi:10.1126/science.1116412.

Mitchell, J. K., G. R. Holdgate, M. W. Wallace, and S. J. Gallagher (2004), Late Neogene strandlines of southern Victoria: A unique record of eustasy and tectonics in southeast Australia, *Aust. J. Earth Sci.*, *52*(2), 279–297, doi:10.1080/08120090500139455.

Moss, G. D., D. L. Cathro, and J. A. Austin, JR (2004), Sequence biostratigraphy of prograding clinoforms, Northern Carnarvon Basin, Western Australia: A proxy for variations in Oligocene to Pliocene global sea level?, *Palaios*, *19*(3), 206–226, 10.1669/0883-1351(2004)019<0206:SBOPCN>2.0.CO;2.

Moucha, R., A. M. Forte, J. X. Mitrovica, D. B. Rowley, S. Quéré, N. A. Simmons, and S. P. Grand (2008), Dynamic topography and long-term sea-level variations: There is no such thing as a stable continental platform, *Earth Planet. Sci. Lett.*, *271*(1-4), 101–108, doi:10.1016/j.epsl.2008.03.056.

Müller, R., C. Gaina, A. Tikku, D. Mihut, S. Cande, and J. Stock (2000a), Mesozoic/Cenozoic tectonic events around Australia, *A. Geophys. Union Mon. 121*, The History and Dynamics of Global Plate Motions, 161–188.

Müller, R. D., V. S. L. Lim, and A. R. Isern (2000b), Late Tertiary tectonic subsidence on the northeast Australian passive margin: response to dynamic topography?, *Mar. Geol.*, *162*(2–4), 337–352, doi:10.1016/S0025-3227(99)00089-4.

Müller, R. D., M. Sdrolias, C. Gaina, and W. R. Roest (2008), Age, spreading rates, and spreading asymmetry of the world's ocean crust, *Geochem. Geophys. Geosyst.*, *9*(4), Q04006, doi:10.1029/2007GC001743.

Panasyuk, S. V., and B. H. Hager (2000), Models of isostatic and dynamic topography, geoid anomalies, and their uncertainties, *J. Geophys. Res.*, *105*(B12), 28, 199–28, 209, doi:10.1029/2000jb900249.

Parsons, B., and J. G. Sclater (1977), An analysis of the variation of ocean floor bathymetry and heat flow with age, *J. Geophys. Res.*, *82*, 803–827, doi:10.1029/JB082i005p00803.

Pigram, C. J., and P. A. Symonds (1991), A review of the timing of the major tectonic events in the New Guinea orogen, *J. Southe. Asian Earth Sci.*, *6*(3-4), 307–318, doi:10.1016/0743-9547(91)90076-A.

Pomar, L. (2001), Types of carbonate platforms: A genetic approach, *Basin Res.*, *13*(3), 313–334, doi:10.1046/j.0950-091x.2001.00152.x.

Ritsema, J., H. J. van Heijst, and J. H. Woodhouse (1999), Complex shear wave velocity structure imaged beneath Africa and Iceland, *Science*, *286*(5446), 1925–1928, doi:10.1126/science.286.5446.1925.

Ritsema, J., A. Deuss, H. J. van Heijst, and J. H. Woodhouse (2010), S40RTS: A degree-40 shear-velocity model for the mantle from new Rayleigh wave dispersion, teleseismic traveltime and normal-mode splitting function measurements, *Geophys. J. Int.*, *184*(3), 1223, doi:10.1111/j.1365-246X.2010.04884.x.

Romine, K. K., J. M. Durrant, D. L. Cathro, G. Bernardel, and M. Apthorpe (1997), Petroleum play element prediction for the Cretaceous-Tertiary basin phase, Northern Carnarvon Basin, *APPEA J.*, *37*, 315–339.

Sandiford, M. (2007), The tilting continent: A new constraint on the dynamic topographic field from Australia, *Earth Planet. Sci. Lett.*, *261*(1-2), 152–163, doi:10.1016/j.epsl.2007.06.023.

Sandiford, M., M. Quigley, P. de Broekert, and S. Jakica (2009), Tectonic framework for the Cenozoic cratonic basins of Australia, *Aust. J. Earth Sci.*, *56*, 5–18, doi:10.1080/08120090902870764.

Schellart, W. P., B. L. N. Kennett, W. Spakman, and M. Amaru (2009), Plate reconstructions and tomography reveal a fossil lower mantle slab below the Tasman Sea, *Earth Planet. Sci. Lett.*, *278*(3-4), 143–151, doi:10.1016/j.epsl.2008.11.004.

Schlager, W. (1999), Scaling of sedimentation rates and drowning of reefs and carbonate platforms, *Geology*, *27*(2), 183–186, 10.1130/0091-7613(1999)027<0183:sosrad>2.3.co;2.

Schlager, W., J. J. G. Reijmer, and A. Droxler (1994), Highstand shedding of carbonate platforms, *J. Sed. Res.*, *64*(3b), 270–281, doi:10.1306/d4267faa-2b26-11d7-8648000102c1865d.

Schubert, G. D., D. L. Turcotte, and P. Olson (2001), *Mantle Convection in the Earth and Planets*, Cambridge University Press, Cambridge, UK. doi:10.1017/CBO9780511612879.

Sclater, J. G., and P. A. F. Christie (1980), Continental stretching: An explanation of the post-mid-Creatceous subsidence of the central North Sea Basin, *J. Geophys. Res.*, *85*(B7), 3711–3739, 10.1029/JB085iB07p03711.

Smith, W. H. F., and D. T. Sandwell (1997), Global sea floor topography from satellite altimetry and ship depth soundings, *Science*, *277*(5334), 1956–1962, doi:10.1126/science.277.5334.1956.

Stein, C. A., and S. Stein, (1992), A model for the global variation in oceanic depth and heat-flow with lithospheric age, *Nature*, *359*(6391), 123–129, doi:10.1038/359123a0.

Steinberge, D. (2007), Effects of latent heat release at phase boundaries on flow in the Earth's mantle, phase boundary topography and dynamic topography at the Earth's surface, *Phys. Earth Planet. In.*, *164*(1-2), 2–20, doi:10.1016/j.pepi.2007.04.021.

Tapley, B., J. Ries, S. Bettadpur, D. Chambers, M. Cheng, F. Condi, B. Gunter, Z. Kang, P. Nagel, R. Pastor, T. Pekker, S. Poole, and F. Wang (2005), GGM02—An improved Earth gravity field model from GRACE, J. *Geodesy*, *79*(8), 467–478, doi:10.1007/s00190-005-0480-z.

Wallace, M. W., J. A. Dickinson, M. Sandiford, and D. H. Moore (2005), Late Neogene strandlines of southern Victoria: A unique

record of eustacy and tectonics in southeast Australia, *Aust. J. Earth Sci.*, *52*(2), 277–295, doi:10.1080/08120090500139455.

Wellman, P., I. McDougall (1974), Cainozoic igneous activity in eastern Australia, *Tectonophysics*, *23*(1-2), 49–65, doi:10.1016/0040-1951(74)90110-3.

Wessel, P., and W. H. F. Smith (1998), New, improved version of Generic Mapping Tools released, *EOS Trans. Am. Geophys. Union*, *79*(47), 579.

Wheeler, P., and N. White (2000), Quest for dynamic topography: Observations from Southeast Asia, *Geology*, *28*(11), 963–966, 10.1130/0091-7613(2000)28<963:qfdtof>2.0.co;2.

White, R. S., D. McKenzie, and R. K. Onions (1992), Oceanic crustal thickness from seismic measurements and rare-earth element inversions, *J. Geophys. Res.*, *97*(B13), 19,683–19,715, doi:10.1029/92JB01749.

Whittaker, J. M., R. D. Müller, and M. Gurnis (2010), Development of the Australian-Antarctic depth anomaly, *Geochem. Geophys. Geosyst.*, *11*(11), Q11006, doi:10.1029/2010GC003276.

Williams, H. D., P. M. Burgess, V. P. Wright, G. Della Porta, and D. Granjeon (2011), Investigating carbonate platform types: Multiple controls and a continuum of geometries, *J. Sed. Res.*, *81*(1), 18–37, doi:10.2110/jsr.2011.6.

Winterbourne, J., A. Crosby, and N. White (2009), Depth, age and dynamic topography of oceanic lithosphere beneath heavily sedimented Atlantic margins, *Earth Planet. Sci. Lett.*, *287*(1-2), 137–151, doi:10.1016/j.epsl.2009.08.019.

Wright, C. A. (1977), Distribution of Cainozoic foraminifera in the Scott Reef no. 1 well, Western Australia, *J. Geol. Soc. Aust.*, *24*(5-6), 269–277, doi:10.1080/00167617708728988.

Wyllie, M. R. J., A. R. Gregory, and L. W. Gardner (1956), Elastic wave velocities in heterogeneous and porous media, *Geophysics*, *21*(1), 41–70, doi:10.1190/1.1438217.

Young, H. C., N. Lemon, and J. Hull (2001), The middle Cretaceous to recent sequence stratigraphic evolution of the Exmouth-Barrow margin, Western Australia, *APPEA J.*, *41*, 381–413.